Sperm chemotaxis is driven by the slope of the chemoattractant concentration field

Ramírez-Gómez H.V.[1], Jiménez-Sabinina V.[2], Tuval I.[3], Velázquez-Pérez M.[1], Beltrán C.[1], Carneiro J.[4], Wood C.D.[1, 5], Darszon A.[1, *], Guerrero A.[1, 5, *].

[1] Departamento de Genética del Desarrollo y Fisiología Molecular, Instituto de Biotecnología, Universidad Nacional Autónoma de México (UNAM), Cuernavaca, Morelos, 62210, México.

[2] Cell Biology and Biophysics Unit, European Molecular Biology Laboratory (EMBL), Heidelberg, Germany.

[3] Mediterranean Institute for Advanced Studies, IMEDEA (CSIC-UIB), Esporles, Balearic Islands, Spain.

[4] Instituto Gulbenkian de Ciência (IGC), Rua da Quinta Grande, 6 2780-156, Oeiras, Portugal.

[5] Laboratorio Nacional de Microscopía Avanzada, Instituto de Biotecnología, Universidad Nacional Autónoma de México (UNAM), Cuernavaca, Morelos, 62210, México.

[*] Correspondence and requests for materials should be addressed to A.G. or A.D. (email: adanog@ibt.unam.mx, darszon@ibt.unam.mx).

Abstract

Spermatozoa are attracted to their conspecific female gamete by diffusive molecules released from the egg investments, a process called chemotaxis. The decapeptide speract induces metabolic and permeability changes in *Strongylocentrotus purpuratus* sea urchin sperm. In spite of decades since speract purification from *S. purpuratus* egg investments, sperm chemotaxis has not been demonstrated in this species. By studying how the stimulus function, which spermatozoa experience during the accumulation of bound chemoattractants throughout their trajectory, influences both their motility response and their internal Ca^{2+} oscillations, we were able to show, for the first time, that *S. purpuratus* spermatozoa exhibit chemotaxis under sufficiently steep speract concentration gradients. We demonstrate that this process arises through frequency entrainment of the coupled metabolic oscillators.

Introduction

Broadcast spawning organisms, such as marine invertebrates, release their gametes into open sea, where they are often subject to extensive dilution that reduces the probability of gamete encounter (Lotterhos, 2010). In many marine organisms, female gametes release diffusible molecules that attract homologous spermatozoa (Lillie, 1913, Miller, 1985, Suzuki, 1995). Propelled by their beating flagella, spermatozoa detect and respond to chemoattractant concentration gradients by steering their swimming trajectory toward the gradient source: the egg. Though it was in bracken ferns where sperm chemotaxis was first identified (Pfeffer, 1884), sea urchins are currently the best-characterized model system for studying sperm chemotaxis at a molecular level (Alvarez et al., 2012, Cook et al., 1994, Darszon et al., 2008, Strunker et al., 2015, Wood et al., 2015).

The sea urchin egg is surrounded by an extracellular matrix which contains short sperm-activating peptides (SAPs), that modulate sperm motility through altering intracellular Ca^{2+} concentration ($[Ca^{2+}]_i$) and other signaling intermediates (Darszon et al., 2008, Suzuki, 1995). The probability of sperm-egg encounter is enhanced by the prompt transduction of the biochemical signals triggered by SAPs into the appropriate reorientation of the sperm trajectory.

The decapeptide speract is one of best characterized members of the SAP family due to its powerful stimulating effect on metabolism, permeability and motility in *S. purpuratus* and *L. pictus* spermatozoa. In 2003, it was shown that the binding of speract to its receptor located in the flagellar plasma membrane, triggers a train of $[Ca^{2+}]_i$ increases in immobilized *S. purpuratus* spermatozoa (Wood et al., 2003). This calcium signal was thought to regulate the activity of dynein motor proteins in the flagellum, thus might modulate the swimming path of sperm (Brokaw, 1979).

A direct link between $[Ca^{2+}]_i$ signaling and sperm motility was established through the use of optochemical techniques to rapidly, and non-turbulently, expose swimming sea urchin spermatozoa to their conspecific attractant in a well-controlled experimental regime (Wood et al., 2005, Bohmer et al., 2005). Currently, it is well established that the transient $[Ca^{2+}]_i$ increases triggered by chemoattractants produce a sequence of turns and straight swimming episodes (turn-and-run), where each turning event results from the rapid increase in the $[Ca^{2+}]_i$ (Wood et al., 2005, Bohmer et al., 2005, Shiba et al., 2008, Alvarez et al., 2012). The turn-and-run seems to be a general requirement for sperm chemotaxis, however it is not sufficient on its own to produce a chemotactic response (Guerrero et al., 2010a, Strunker et al., 2015, Wood et al., 2007, Wood et al., 2005).

Our current understanding of chemotaxis, suggests that sperm first sample the chemoattractant concentration gradient by swimming in periodic paths (either circular 2D or helical 3D). During the sampling phase, the accumulation of bound chemoattractants triggers $[Ca^{2+}]_i$ transients that control the waveform of the flagellar beat. In this way, the alternate periods of asymmetrical (turn) and symmetrical (run) flagellar beating give rise to a looping swimming pattern that guides up to the source of the chemoattractant gradient.

Friedrich and Jülicher proposed a generic theory that captures the essence of sperm navigation following periodic paths in a non-homogeneous chemoattractant field, where the sampling of a periodic concentration stimulus *s(t)* is translated by intracellular signaling *i(t)* into the periodic modulation of the swimming path curvature *k(t)* (Friedrich and Jülicher, 2007, Friedrich and Jülicher, 2008). As result, the periodic swimming path drifts in a direction that depends on the internal dynamics of the

81 signaling system. In this theory, the latency of the intracellular signaling (the $[Ca^{2+}]_i$
82 signal), expressed as the phase shift between *s(t)* and *k(t)*, is a crucial determinant of the
83 directed looping of the swimming trajectory up the chemical concentration field. This
84 theory also predicts that chemotaxis is a robust property of the system that does not
85 require fine-tuning of parameters (if the signaling system is adaptive) (Friedrich and
86 Jülicher, 2008, Friedrich and Jülicher, 2009). In other words, there is a large range of
87 parameters for which sperm chemotaxis is a robust outcome, providing an effective way
88 for sampling the local chemoattractant concentration field and detecting the direction of
89 the concentration gradient (Kaupp et al., 2003, Kashikar et al., 2012, Pichlo et al., 2014,
90 Friedrich and Jülicher, 2008, Friedrich and Jülicher, 2007).

91 Even though the conceptual framework of Friedrich & Jülicher provides insights into
92 the mechanism governing sperm chemotaxis, it does not explore the scenario whereby
93 chemoattractants trigger an autonomous $[Ca^{2+}]_i$ oscillator operating in the absence of a
94 periodic stimulus. The existence of an autonomous $[Ca^{2+}]_i$ oscillator triggered by
95 chemoattractants (Wood et al., 2003, Espinal et al., 2011, Aguilera et al., 2012) suggests
96 that sperm chemotaxis might operate in a dynamical space where two autonomous
97 oscillators, namely the stimulus function and the internal Ca^{2+} oscillator, reach
98 frequency entrainment (Pikovsky et al., 2001).

99 In spite of 30 years of research since speract's isolation from *S. purpuratus* oocytes
100 (Hansbrough and Garbers, 1981, Suzuki, 1995), chemotaxis of *S. purpuratus* sperm
101 towards this peptide has not yet been demonstrated (Cook et al., 1994, Darszon et al.,
102 2008, Guerrero et al., 2010b, Kaupp, 2012, Miller, 1985, Wood et al., 2015). A
103 comparison between individual *L. pictus* and *S. purpuratus* sperm responses to a
104 specific chemoattractant concentration gradient generated by photoactivating caged
105 speract (CS) revealed that only *L. pictus* spermatozoa exhibit chemotaxis under these

conditions (Guerrero et al., 2010a). In that study, *L. pictus* spermatozoa experience $[Ca^{2+}]_i$ fluctuations and pronounced turns while swimming in descending speract gradients, that result in spermatozoa reorienting their swimming behavior along the positive chemoattractant concentration gradient. In contrast, *S. purpuratus* spermatozoa experience similar trains of $[Ca^{2+}]_i$ fluctuations that in turn drive them to relocate, but with no preference towards the center of the chemoattractant gradient (Guerrero et al., 2010a).

The precise triggering of $[Ca^{2+}]_i$ fluctuations associated to sperm turning events towards the chemoattractant gradient, as well as the turn-and-run behavior seem to be general requirements for sperm chemotaxis in marine invertebrates (Bohmer et al., 2005, Guerrero et al., 2010a, Jikeli et al., 2015, Kashikar et al., 2012, Shiba et al., 2008, Strunker et al., 2015, Wood et al., 2015), and could be important features of sperm chemotaxis in general.

In the present work, we investigate whether *S. purpuratus* spermatozoa can undergo chemotaxis. Particularly, we examined whether there is a physical limit to the sampling of the chemoattractant concentration gradient needed for detection that has, to date, prevented observation and characterization of their chemotactic response. We report that *S. purpuratus* spermatozoa are chemotactic only when exposed to much steeper speract concentration gradients than those previously employed. Furthermore, we explored the coupling between the recruitment of speract molecules during the sperm voyage, the triggered signaling cascade and the internal Ca^{2+} oscillator; and demonstrate that sperm chemotaxis arises through coupled metabolic oscillators.

Results

Chemotaxis refers to the directed movement of an organism or a cell in a chemical gradient. The first step in a chemotactic response is the sampling of a chemoattractant field, from where in a given time *T*, statistical fluctuations limit the precision with which the searcher can determine the concentration of the chemoattractant (Berg and Purcell, 1977, Vergassola et al., 2007, Dusenbery, 2011).

Assuming that the number of ligands that collide with a single receptor per unit of time is proportional to radius of the receptor *s*, the concentration of the attractant *c* and the diffusion constant of the attractant *D*, the total number of collisions between N_R receptors in a time interval T is $x = N_R sDcT$. The statistical fluctuation on the number of ligand-receptor collisions *x* follows a Poisson distribution, and therefore the expected value $E[x]$ and the variance $Var[x]$ are the same. In this scenario, the coefficient of variation is $\frac{SD[x]}{E[x]} = \frac{\sqrt{Var[x]}}{E[x]} = \frac{\sqrt{E[x]}}{E[x]}$. This coefficient can be interpreted as the smallest fractional error attainable in the determination of the concentration of the attractant (see **Theory** section) (Berg and Purcell, 1977, Dusenbery, 2011, Vergassola et al., 2007).

$$u_1 = (N_R sDcT)^{-1/2} \qquad (1)$$

Uncertainty in the determination of the presence of chemoattractant molecules

The flagella of sea urchin spermatozoa possess a large number of high affinity SAP receptors (10^4-10^6 depending on species and author) (Nishigaki and Darszon, 2000, Shimomura and Garbers, 1986, Smith and Garbers, 1982, Kaupp et al., 2008). This great number of SAP receptors provides spermatozoa with a fine-tuned sensory system able to respond to a wide range of SAP concentrations (10^{-12}-10^{-6} M). That these receptors are distributed along the entire flagellum increases the probability of capturing even a few arriving molecules (Kaupp et al., 2003, Kashikar et al., 2012).

153 To understand the theoretical sampling capabilities of sea urchin spermatozoa, given
154 a specific speract concentration (in a homogeneous concentration field), and flagellar
155 receptor availability, we first computed the smallest fractional error attainable in the
156 detection of a chemoattractant u_1 at different concentrations, considering distinct
157 receptor numbers. A theoretical *S. purpuratus* spermatozoon possessing N_R = 2 x 10^4
158 receptors, will sample a medium containing 10 nM of speract in time T = 0.5 s with an
159 uncertainty of u_1 = 0.006 (**Figure 1 – figure supplement 1a** and **Figure 1 – table**
160 **supplement 1**). Here, the time scale T was considered as the time needed for a *S.*
161 *purpuratus* spermatozoon to traverse a distance equivalent to approximately half a
162 circumference of its circular trajectory when confined to the water-glass boundary, in a
163 homogeneous field of speract. The least fractional error attainable in the determination
164 of the concentration of the attractant has no upper boundary, however u_1 values greater
165 than 1 indicates that stochastic fluctuations dominate over the signal (Berg and Purcell,
166 1977). For simplicity, u_1 was considered to operate in the range [0, 1]. In other words,
167 our model spermatozoon, when exposed to a chemoattractant concentration of 10 nM,
168 will be able to determine the presence of speract molecules with 0.6% of uncertainty in
169 0.5 s.

170 If the spermatozoon finds itself in a sampling space of 1 pM of speract, this level of
171 uncertainty increases to 60% over the same interval. It is likely that at speract
172 concentrations below picomolar, an *S. purpuratus* spermatozoon will require relatively
173 extended sampling times to determine the presence of speract molecules. For example,
174 for a spermatozoon sampling a 1 pM concentration field of speract for 60 seconds, the
175 uncertainty of receptor occupancy drops to 6% (**Figure 1 – figure supplement 1b**).

176 An important difference between *S. purpuratus* and *L. pictus* spermatozoa is their
177 respective receptor density; the former possesses 3.15x fewer receptors than the latter (2

x 10^4 versus 6.3 x 10^4 receptors per cell, respectively) (**Figure 1 – table supplement 1**) (Nishigaki and Darszon, 2000, Nishigaki et al., 2001). Note that if *S. purpuratus* spermatozoa were to possess a receptor density equivalent to *L. pictus*, they would be able to sample a speract concentration field of 1 pM within 0.5 seconds with an uncertainty of u_1 = 0.4 (40%) (**Figure 1 – figure supplement 1a**). Given the differences in sensitivities between these two species, the lack of chemotactic responses in *S. purpuratus* spermatozoa could possibly be explained, at least partially, by their lesser density of speract receptors, compared to *L. pictus*.

Uncertainty in the determination of sperm position in a non-homogeneous chemoattractant concentration field

To detect a chemoattractant concentration gradient, the signal at two given points, sampled throughout a time interval must be greater than the noise, which in this case would arise from spontaneous stochastic activation of one or more components of the chemoattractant signaling pathway (**Figure 1a**) (Berg and Purcell, 1977, Vergassola et al., 2007, Wood et al., 2015, Dusenbery, 2011). Information regarding the direction of the chemoattractant gradient results from the magnitude difference of the signal at two sampled positions (for further explanation see **Theory** section). The smallest fractional error in determination of the chemoattractant gradient direction due to the occupation state of receptors is:

$$u_2 = v^{-1}T^{-3/2}(N_R s D)^{-1/2} c^{1/2} \varepsilon^{-1} \qquad (2)$$

where v is the swimming velocity and $\varepsilon = dc/dr$ is the chemoattractant concentration gradient (**Figure 1a**) (Berg and Purcell, 1977, Dusenbery, 2011, Vergassola et al., 2007). A locality requirement must also be met: the change in concentration across the distance spanned during T must be small, compared to the concentration itself

(Vergassola et al., 2007).

The slope of the chemoattractant concentration gradient ε directly impinges on the ability to reliably determine the source of the attractant (**Figure 1b**). At high concentrations of speract (10^{-8} to 10^{-6} M) the change in receptor occupancy experienced by *S. purpuratus* spermatozoa, at two given distinct locations, allows the reliable assessment of the chemical gradient, when $u_2 < 0.05$ (**Figure 1b**) (As for u_1, u_2 was considered to operate in the range [0, 1]) (Vergassola et al., 2007, Berg and Purcell, 1977). However, at low concentrations of speract (below of 10^{-9} M), where other parameters are identical, stochastic fluctuations tend to dominate over the signal (**Figure 1b**). Under these low-concentration regimes, the slope of the chemoattractant gradient is determinant; shallow gradients ($\varepsilon < 10^{-12}$ M μm^{-1}) increase the uncertainty for detection of gradient polarity. In contrast, steeper chemoattractant gradients, *i.e.* $\varepsilon \geq 10^{-11}$ M μm^{-1}, would allow *S. purpuratus* spermatozoa to determine the orientation of the chemical gradient dependably (**Figure 1b**).

Previously it was shown that *L. pictus* spermatozoa experience chemotaxis in response to exposure to a gradient of speract (Guerrero et al., 2010a). Notably, under the same experimental regime *S. purpuratus* spermatozoa undergo a motility response to the presence of speract, yet do not demonstrate chemotaxis. It seems reasonable to speculate that the lack of chemotactic responses in *S. purpuratus* spermatozoa is due to their reduced receptor density relative to *L. pictus* spermatozoa. The chemoreception model predicts that, in contrast to *L. pictus*, *S. purpuratus* spermatozoa might determine the direction of the attractant gradient in the range of 10^{-10} to 10^{-9} M (**Figure 1b**, orange and yellow lines with $u_2 < 5\%$), and thus can only determine the orientation of the chemical gradient in steep, but not shallow concentration gradients (**Figure 1b**, yellow and cyan lines with $u_2 < 5\%$). If the latter holds to be true, then the model predicts that

S. purpuratus spermatozoa should be able to experience chemotaxis when exposed to relatively steep speract gradients, which have not been tested experimentally to date.

The ratio of uncertainties for reliable assessment of the direction of a speract gradient between *S. purpuratus* and *L. pictus* spermatozoa can be expressed as:

$$\frac{u_{2\ purpuratus}}{u_{2\ pictus}} = S\frac{\varepsilon_{pictus}}{\varepsilon_{purpuratus}},$$

$$S = \left(\frac{v_{purpuratus}}{v_{pictus}}\right)^{-1}\left(\frac{T_{purpuratus}}{T_{pictus}}\right)^{-3/2}\left(\frac{N_{R\ purpuratus}}{N_{R\ pictus}}\right)^{-1/2} \quad (3, 4)$$

with *S* being a factor that scales the slope of the speract gradient to a regime that allows *S. purpuratus* spermatozoa to detect the local direction of the chemical gradient. In other words, the model predicts that *S. purpuratus* spermatozoa should undergo chemotaxis in a speract gradient approximately three times steeper than the gradient that drives chemotaxis in *L. pictus* spermatozoa, with $\varepsilon_{\text{purpuratus}} = 3.25\ \varepsilon_{\text{pictus}}$.

In summary, the chemoreception model suggests that *S. purpuratus* spermatozoa detect chemoattractant gradients with less sensitivity than those of *L. pictus*. It also predicts that *S. purpuratus* spermatozoa may detect chemoattractant gradients in the 10^{-9} M regime with sufficient certainty only if the difference in sampling concentration is greater than 10^{-11} M µm^{-1} (steep concentration gradients) (**Figure 1b**). Given this prediction, we designed and implemented an experimental condition where *S. purpuratus* spermatozoa should experience chemotaxis.

S. purpuratus spermatozoa accumulate at steep speract concentration gradients

Our experimental setup is designed to generate specific concentration gradients by focusing a brief (200 ms) flash UV light along an optical fiber, through the objective, and into a field of swimming *S. purpuratus* spermatozoa containing CS at 10 nM in artificial sea water (Tatsu et al., 2002, Guerrero et al., 2010a). To test experimentally whether *S. purpuratus* undergo chemotaxis, as predicted from the chemoreception

model, we varied the slope of the chemoattractant gradient by separately employing four optical fibers of distinct diameters that could be arranged into five different configurations (*f1, f2, f3, f4, f5*).

Each configuration produces a characteristic pattern of UV illumination within the imaging field (**Figure 2**). The UV intensity was measured at the back focal plane of the objective for each fiber configuration (**Figure 2a** and **Figure 2 – table supplement 1**). The spatial derivative of the imaged UV light profile was computed for use as a proxy for the slope of the speract concentration gradient (**Figure 2b**). By examining these UV irradiation patterns, we calculated that, at the gradient peak, the highest concentration of speract released through photo-liberation from CS is generated by the *f5* fiber, followed by *f4* > *f3* > *f2* > *f1*. The steepest UV irradiation gradients are those generated by the *f2*, *f3* and *f5* fibers (**Figure 2b**).

Irrespective of the optical fiber used, the photo-activation of caged speract triggers the stereotypical Ca^{2+}-dependent motility responses of *S. purpuratus* spermatozoa **(Figure 2c, Movies 1, 2, 5, 6** and **7**). To determine whether these changes lead to sperm accumulation, we developed an algorithm which automatically scores the number of spermatozoa at any of four defined concentric regions (R1, R2, R3, and R4) relative to the center of the speract concentration gradient (**Figure 2 – figure supplement 1**).

Photo-liberation of speract through either *f2* or *f3* fiber, but not through *f1*, *f4* or *f5* fibers, lead to the accumulation of *S. purpuratus* spermatozoa towards the center of the speract gradient (zones R1 and R2) within the first 5-10 seconds after UV irradiation (**Figure 3**, **Figure 3 - figure supplement 1, Figure 3 - figure supplement 2**, **Movies 1**, and **2**).

Interestingly, for *f2*, the number of spermatozoa increases in R1 and R2 and decreases in R3 and R4, indicating that cells from the R3 and R4 regions most probably

278 relocate towards R1 and R2 (**Figure 3a**, **Figure 3 - figure supplent 2** and **Movie 1**). In
279 the case of the *f3* gradient, the number of spermatozoa increases in the R1, R2 and R3
280 regions and decreases in the R4 region, suggesting that spermatozoa in R4 and possibly
281 outside of the imaged field are entering the other regions (**Figure 3a** and **Movie 2**). The
282 maximum sperm accumulation (about two-fold) occurs in R1 for the *f3* gradient (**Figure**
283 **3a** and **Movie 2**).

284 In the case of exposure to the *f5* speract concentration gradient the number of
285 spermatozoa showed a tendency to increase in R2, R3 and R4, although it was only
286 statistically significant in R4 (**Figure 3a**, **Figure 3 - figure supplement 2** and **Movie**
287 **6)**. Gradients *f1, f4* and negative controls (Low $[Ca^{2+}]_i$ or High $[K^+]_e$) did not show
288 increased sperm number in any region (**Figure 3a**, **Figure 3 - figure supplement 1**,
289 **Figure 3 - figure supplement 2**, **Movies 3**, **4**, **5** and **6**).

290 We also evaluated the corresponding $[Ca^{2+}]_i$ changes across the imaging field for
291 each imposed speract concentration gradient. Gradients *f2* to *f5* increase $[Ca^{2+}]_i$ in
292 spermatozoa at least two-fold, while the increase for the *f1* gradient was modest (**Figure**
293 **3b**). Interestingly, $[Ca^{2+}]_i$ levels rose highest upon exposure to the *f4* gradient, even
294 though the number of spermatozoa did not increase significantly (**Figure 3a**), which
295 underlines the notion that elevated $[Ca^{2+}]_i$ levels are necessary, but not sufficient to
296 drive the accumulation of spermatozoa (**Figure 3**), as previously suggested (Kaupp et
297 al., 2003, Wood et al., 2005, Bohmer et al., 2005, Guerrero et al., 2010a, Alvarez et al.,
298 2012).

299 In summary, *S. purpuratus* spermatozoa accumulate towards the center of the speract
300 gradients generated by the *f2*- and *f3*-fibers, which are the two optical fibers that
301 generate UV light profiles with steeper slopes compared to the *f1* and *f4* fibers (**Figure**
302 **2b**). Notably, use of fibers *f4* and *f5* photo-releases higher concentrations of speract (by

303 providing higher UV energies than other fibers) (**Figure 2a, Figure 2 table**
304 **supplement 1**), yet they trigger neither the maximum accumulation of *S. purpuratus*
305 spermatozoa at the center of the chemoattractant field, nor the most elevated $[Ca^{2+}]_i$
306 response.
307
308 ***S. purpuratus spermatozoa undergo chemotaxis upon exposure to steep speract***
309 ***gradients***
310 The spatial derivative of the UV profiles shown in **Figure 2b** indicates that the
311 steeper light gradients generated from UV irradiation are those of *f2, f3* and *f5*, which
312 are assumed to generate the most pronounced speract gradients of similar form. This
313 assumption is strictly only valid at the instant of UV exposure, as subsequently the
314 speract gradient dissipates over time with a diffusion constant of $D \approx 240\ \mu m^2\ s^{-1}$.
315 We further sought to understand how the stimulus function, which *S. purpuratus*
316 spermatozoa experience during the accumulation of bound speract throughout their
317 trajectory, influences their motility response. For this purpose, we computed the spatio-
318 temporal dynamics of the speract gradient for *f1, f2, f3, f4* and *f5* fibers (**Figure 4a, b**
319 and **Figure 4 - figure supplement 1**) and analyzed the trajectories of spermatozoa
320 swimming in these five distinct speract gradient configurations (**Figure 4c** and **Figure 4**
321 **- figure supplement 2**). From these trajectories, we derived the chemotaxis indices
322 (LECI, (Yoshida et al., 2002)) (**Figure 4d** and **Figure 5**), and computed the stimulus
323 function of individual spermatozoa in response to each of the five speract gradient
324 forms (**Figure 4e** and **Figure 4 - figure supplement 2**).
325 Fibers *f2, f3* and *f5* triggered chemotaxis in *S. purpuratus* spermatozoa (**Figure 4**,
326 **Figure 4 - figure supplement 2** and **Figure 5**). Under such conditions, only those
327 spermatozoa located in the regions R3 and R4 at the moment of speract uncaging

underwent chemotaxis (**Figure 5**; see **Figure 4** and **Figure 4 - supplement figure 2** for single sperm reorienting towards the center of speract gradients generated by the *f2* and *f3* fibers, respectively). For both, *f2* and *f3* conditions, sperm chemotaxis initiated within the first 3 s after speract exposure, and lasted less than 10 s (**Figure 5**, **Figure 3 - figure supplement 1**, **Movies 1** and **2**).

Figure 4b shows that, for the *f2* condition, the slope of the speract gradient within R2 and regions is barely altered during the initial 3 seconds of speract exposure (gray shading). Spermatozoa in that region sample a pseudo-static speract gradient over a short (2-3 s) period, which is apparently sufficient to permit detection of the direction of the gradient. In contrast, spermatozoa located at other regions (R1, R3, R4) experience a speract gradient with a slope that changes during the sampling time (**Figure 4a**, **4b**).

In summary, *f2*, *f3* and *f5* optical fibers generate speract concentration gradients that drive the accumulation of *S. purpuratus* spermatozoa. Of note, the *f4* fiber generates a speract gradient that activates motility responses of *S. purpuratus* spermatozoa but not chemotaxis (**Movie 6**), although it was previously shown that it triggers the accumulation of *L. pictus* spermatozoa (Guerrero et al., 2010a).

The model of chemoreception presented in the previous section (**equations (3, 4)**) predicts a scaling rule for chemotactic responses between *S. purpuratus* and *L. pictus* spermatozoa of $S > 3.25$. Moreover, the UV-irradiation profiles shown in **figure 2b** indicate that *f2*, *f3*, and *f5* fibers generate steeper speract gradients than *f4* fiber.

To reliably determine the direction of the chemoattractant concentration gradient, the signal difference *dc* between two sampled positions *dr* must be greater than the noise (**Figure 1a**). In order to test the prediction of the chemoreception model, we computed the local relative slope ξ detected by single spermatozoa exposed to a given speract concentration gradient, with $\xi = c^{-1/2} dc/dr$ (**Figure 4e**).

We found that, in agreement with the chemoreception model, the maximum relative slope $\xi_{max} = Max(\xi_1, \xi_2, \xi_3, ..., \xi_n)$ experienced by *S. purpuratus* spermatozoa, when exposed to *f2* and *f3* speract gradients, were up to 2-3 times greater than that experienced when exposed to the *f4*-generated speract gradient (**Figure 6a**). In addition, they were also up to 2-3 times greater than the relative slope experienced by *L. pictus* spermatozoa when exposed to *f4* speract gradient (**Figure 6a**), hence supporting the predicted scaling rule for the detection of the speract concentration gradient between *L. pictus* and *S. purpuratus* spermatozoa.

The slope of the speract gradient is the critical determinant for the strength of coupling between the stimulus function and the internal Ca^{2+} oscillator

To test the idea that the slope of the speract gradient regulates the coupling between the stimulus function and the internal Ca^{2+} oscillator triggered by speract, we made use of a generic model for coupled phase oscillators (Pikovsky et al., 2001). In its simplest form, the model describes two phase oscillators of intrinsic frequencies ω_1 and ω_2 coupled with a strength γ through the antisymmetric function of their phase difference $\phi = \varphi_1 - \varphi_2$. The time evolution of ϕ then follows an Adler equation $d\phi/dt = \Delta\omega - 2\gamma \sin(\phi)$, which is the leading order description for weakly-coupled non-linear oscillators. In the present case, the two coupled oscillators are the internal Ca^{2+} oscillator and the oscillations in the stimulus function induced in spermatozoa swimming across a speract gradient. The former occurs even for immotile cells, for which there are no stimulus oscillations under a spatially uniform speract field (**Figure 6 - supplement 1,** and **Movie 8**); while the later exists under two tested negative controls: cells swimming in Low Ca^{2+} and in High K^+ artificial sea water, both of which inhibit Ca^{2+} oscillations (see **Figure 3, Movie 3** and **4).**

There are two immediate predictions from the Adler model: first, there is a minimum coupling strength necessary for the two oscillators to synchronize ($\gamma_{min} = \Delta\omega/2$). For weaker coupling (*i.e.* $\gamma < \gamma_{min}$), the two oscillators run with independent frequencies and, hence, the phase difference increases monotonically with time; second, and within the synchronous region (*i.e.* $\gamma > \gamma_{min}$), the phase difference between the oscillators is constant and it does not take any arbitrary value, but rather follows a simple relation to the coupling strength ($\phi_{sync} = arcsin(\Delta\omega/2\gamma)$). **Figure 6b** shows the two regions in the parameter space given by $\Delta\omega$ and γ. The boundary between these two regions corresponds to the condition $\gamma = \gamma_{min}$ and it delimits what is known as an Arnold's tongue.

We measure the difference in intrinsic frequency by looking at the instantaneous frequency of the internal Ca^{2+} oscillator just before and after the speract gradient is established. The range of measured $\Delta\omega$ is shown in the same figure as a band of accessible conditions in our experiments (mean of $\Delta\omega$, black line; mean ± standard deviation, green dashed lines). If the driving coupling force between the oscillators is the maximum slope of the speract gradient, *i.e.* $\gamma = \xi_{max}$, we would expect to find a minimum slope ($\overline{\xi^*_{max}}$) below which no synchrony is observed.

This is indeed the case as clearly shown in **Figure 6a**, **6c** and **6d** (magenta line). Moreover, and for cells for which synchronization occurs, the measured phase difference is constrained by the predicted functional form of $\phi_{sync} = \phi_{sync}(\Delta\omega, \gamma)$ as can be verified from the collapsed data shown in **Figure 6c**, and **6d** within the theoretical estimates.

Altogether, the excellent agreement of this simple model of coupled phase oscillators with our data, points to the slope of the speract gradient as the driving force behind the observed synchronous oscillations and, as a result, for the chemotactic ability of sea

403 urchin spermatozoa.

Discussion

Marine spermatozoa, together with many motile microorganisms, explore their environment via helical swimming paths, whereupon encountering a surface these helices collapse to circular trajectories. The intrinsic periodicity of either swimming behavior commonly results in the periodic sampling of the cells chemical environment with direct implications for their ability to accurately perform chemotaxis.

A strict requirement for sperm chemotaxis is the presence of extracellular Ca^{2+}. For chemotaxis to occur, the timing of the Ca^{2+} transients (*i.e.* the intracellular Ca^{2+} oscillations) triggered by the chemoattractants must also be kept in phase with the polarity of the chemoattractant concentration field, which in this, and other studies, is referred as the stimulus function (Bohmer et al., 2005, Guerrero et al., 2010a, Kaupp et al., 2008, Friedrich and Jülicher, 2008). This requisite coupling ensures that the turning events start at the descending phase of the chemoattractant concentration field; otherwise spermatozoa are driven away by Ca^{2+}-dependent motility adjustments. The periodic sampling of chemoattractants by the sperm flagellum continuously feeds back to the signaling pathway governing the intracellular Ca^{2+} oscillator, hence providing a potential coupling mechanism for sperm chemotaxis. Indirect evidence for the existence of a feedback loop operating between the stimulus function and the Ca^{2+} oscillator triggered by chemoattractants has been found in *L. pictus*, *A. punctulata* and *Ciona intestinalis* species, whose spermatozoa show robust chemotactic responses towards their conspecific chemoattractants (Guerrero et al., 2010a, Shiba et al., 2008, Jikeli et al., 2015, Bohmer et al., 2005).

For almost three decades, chemotaxis had not been observed for the widely studied *S. purpuratus* species under diverse experimental conditions, raising doubts about their capabilities to ‘sense’ and respond to the spatial cues provided by the speract

429 concentration gradients. To tackle whether *S. purpuratus* spermatozoa are able to
430 'sense' a chemoattractant concentration gradient, we use a model of chemoreception
431 developed by Berg and Purcell, which considers the minimal requirements needed for a
432 single searcher (*i.e.* a sperm cell) to gather sufficient information to determine the
433 orientation of a non-uniform concentration field. By considering the difference between
434 *L. pictus* and *S. purpuratus* spermatozoa in terms of the number of chemoattractant
435 receptors, receptor pocket size, sampling time, swimming velocity, sampling distance,
436 and the local mean and slope of the chemoattractant concentration field, we predicted
437 that *S. purpuratus* should be able to detect the polarity of a speract concentration field.
438 The model predicts that speract gradient necessary to guide *S. purpuratus* spermatozoa
439 would be up to three times steeper than the gradient that drives chemotactic responses
440 on *L. pictus* spermatozoa. We tested this prediction experimentally by exposing *S.*
441 *purpuratus* spermatozoa to various defined speract concentration gradients. We show
442 that *S. purpuratus* spermatozoa exhibit chemotactic responses but, as predicted by the
443 chemoreception model, only if the speract concentration gradients are sufficiently steep
444 (*i.e.* speract gradients that are at least three times steeper than the speract concentration
445 gradient that drives chemotaxis in *L. pictus* spermatozoa). The shallower speract
446 gradients previously tested are therefore unable to generate any chemotactic response in
447 *S. purpuratus* spermatozoa.

448 To investigate further the molecular mechanism involved in sperm chemotaxis, we
449 measured both the stimulus function and the triggered-internal Ca^{2+} oscillations for up
450 to five hundred *S. purpuratus* spermatozoa exposed to five distinct speract
451 concentration gradients. We demonstrate that the slope of the chemoattractant
452 concentration field is a major determinant for sperm chemotaxis in *S. purpuratus*, and
453 might be an uncovered feature of sperm chemotaxis in general. A steep slope of the

454 speract gradient entrains the frequencies of the stimulus function and the internal Ca^{2+}
455 oscillator triggered by the periodic sampling of a non-uniform speract concentration
456 field. We assessed the transition boundary of the coupling term (the slope of the speract
457 concentration field) for the two oscillators to synchronize, and found it to be very close
458 to the boundary where *S. purpuratus* start to experience chemotaxis. The agreement of
459 our data with a model of weakly coupled phase oscillators, points to the slope of the
460 speract gradient as the driving force behind the observed synchronous oscillations and,
461 as a result, for the chemotactic ability of sea urchin spermatozoa.

462 One can further hypothesize about the evolutionary origin of the described
463 differences in sensitivity to chemoattractant concentration gradients between *S.*
464 *purpuratus* and *L. pictus* spermatozoa given the significant differences between their
465 ecological reproduction niches. The turbulent environment where sea urchin reproduce
466 directly impinges on the dispersion rates of small molecules such as speract, hence,
467 imposing ecological pressure against sperm chemotaxis. For instance, the reproduction
468 success of *L. pictus, S. purpuratus* and *Abalone* species has been shown to peak at
469 particular hydrodynamic shearing values (Zimmer and Riffell, 2011, Riffell and
470 Zimmer, 2007, Mead and Denny, 1995, Hussain et al., 2017). We might ask what are
471 the typical values of the chemoattractant gradients encountered by the different species
472 in their natural habitats. The correct scale to consider when discussing the small-scale
473 distribution of chemicals in the ocean is the Batchelor scale, $l_B = (\eta D^2/\zeta)^{1/4}$, where η is
474 kinematic viscosity, D the molecular diffusivity and ζ is the turbulent dissipation rate
475 (Batchelor, 2006, Aref et al., 2014). Turbulence stirs dissolved chemicals in the ocean,
476 stretching and folding them into sheets and filaments at length scales down to the
477 Batchelor scale: below 1_B molecular diffusion dominates and chemical gradients are
478 smoothened out.

479 *S. purpuratus* is primarily found in the low intertidal zone. The purple sea urchin
480 thrives amid strong wave action and areas with churning aerated water. These more
481 energetic zones, including tidal channels and breaking waves, generate relatively high
482 levels of turbulence ($\zeta \sim 10^{-4}$ m^2s^{-3}) which lead to relatively small values of l_B and,
483 hence, to steep gradients (*i.e.* l/l_B). *L. pictus*, on the contrary, is mostly found at the edge
484 of or inside kelp beds, well below the low tide mark where the levels of turbulence are
485 much more moderate ($\zeta \sim 10^{-6}$ m^2s^{-3}) (Jiménez, 1997, Thorpe, 2007). This difference in
486 turbulent kinetic energy dissipation rate has a significant effect on the largest chemical
487 gradients available in a particular habitat for sperm chemotaxis. The ratio of l_B for the
488 different habitats scales as $l_{Bpurpuratus}/l_{Bpictus} \sim (\zeta_{pictus}/\zeta_{purpuratus})^{1/4} \sim 3$, which fits
489 considerably well with the relative sensitivity to speract of the two species.
490 Furthermore, we have shown that *S. purpuratus* spermatozoa experience chemotaxis
491 toward steeper speract gradients than those that guide *L. pictus* spermatozoa, which is
492 also compatible with the distinct chemoattractant gradients they might naturally
493 encounter during their voyage searching for the egg.

494 The chemoattractant concentration gradients generated in the present study were
495 near-instantaneously set up by the photo-release of speract in still water. Further
496 experimental studies are needed to assess the chemotactic ability of sea urchin
497 spermatozoa to more realistic chemoattractant gradients (as those shaped, for instance,
498 by hydrodynamic forces in their natural environment) and to shed light into the
499 mechanisms governing chemotaxis and their ecological implications.

500

Materials and Methods

Materials

Undiluted *S. purpuratus* or *L. pictus* spermatozoa (Pamanes S. A. de C. V., Ensenada, Mexico and Marinus Scientific, LLC. Newport Beach, CA, USA respectively) were obtained by intracoelomic injection of 0.5 M KCl and stored on ice until used within a day. Artificial seawater (ASW) was 950 to 1050 mOsm and contained (in mM): 486 NaCl, 10 KCl, 10 $CaCl_2$, 26 $MgCl_2$, 30 $MgSO_4$, 2.5 $NaHCO_3$, 10 HEPES and 1 EDTA (pH 7.8). For experiments with *L. pictus* spermatozoa, slightly acidified ASW (pH 7.4) was used to reduce the number of spermatozoa experiencing spontaneous acrosome reaction. Low Ca^{2+} ASW was ASW but pH 7.0 and with 1 mM $CaCl_2$, and Ca^{2+}-free ASW was ASW with no added $CaCl_2$. [Ser5; nitrobenzyl-Gly6]speract, referred to throughout the text as caged speract (CS), was prepared as previously described (Tatsu et al., 2002). Fluo-4-AM and pluronic F-127 were from Molecular Probes, Inc. (Eugene, OR, USA). PolyHEME [poly(2-hydroxyethylmethacrylate)] was from Sigma-Aldrich (Toluca, Edo de Mexico, Mexico).

Loading of Ca^{2+}-fluorescent indicator into spermatozoa

Undiluted spermatozoa were suspended in 10 volumes of low Ca^{2+} ASW containing 0.2% pluronic F-127 plus 20 µM of fluo-4-AM and incubated for 2.5 h at 14 ºC. Spermatozoa were stored in the dark and on ice until use.

Imaging of fluorescent swimming spermatozoa

The cover slips were briefly immersed into a 0.1% wt/vol solution of poly-HEME in ethanol, hot-air blow-dried to rapidly evaporate the solvent and mounted on reusable chambers fitting a TC-202 Bipolar temperature controller (Medical Systems Corp.). The temperature plate was mounted on a microscope stage (Eclipse TE-300; Nikon) and

maintained at a constant 15 ºC. Aliquots of labeled sperm were diluted in ASW and transferred to an imaging chamber (final concentration ~$2x10^5$ cells ml^{-1}). Epifluorescence images were collected with a Nikon Plan Fluor 40x 1.3 NA oil-immersion objective using the chroma filter set (ex HQ470/40x; DC, 505DCXRU; em, HQ510LP) and recorded on a DV887 iXon EMCCD Andor camera (Andor Bioimaging, NC). Stroboscopic fluorescence illumination was supplied by a Cyan LED no. LXHL-LE5C (Lumileds Lighting LLC, San Jose, USA) synchronized to the exposure output signal of the iXon camera (2 ms illumination per individual exposure). Images were collected with AndoriQ 1.8 software (Andor Bioimaging, NC) at 30.80 fps in full-chip mode (observation field of 200 x 200 µm).

Image processing

The background fluorescence was removed by generating an average pixel intensity time-projection image from the first 94 frames before uncaging, which was then subtracted from each frame of the image stack by using the Image calculator tool of ImageJ 1.49u (Schneider et al., 2012). For **Figure 2c**, the maximum pixel intensity time projections were created every 3 s from background-subtracted images before and after the UV flash.

Quantitation of global changes of spermatozoa number and $[Ca^{2+}]_i$

To study the dynamics of overall sperm motility and $[Ca^{2+}]_i$ signals trigger by the distinct speract gradients, we developed an algorithm that provides an efficient approach to automatically detect the head of every spermatozoa in every frame of a given video-microscopy (C/C++, OpenCV 2.4, Qt-creator 2.4.2). Fluorescence microscopy images generated as described previously were used. The following steps summarize the work-flow of the algorithm (**Figure 2 - figure supplement 1**):

1. Segment regions of interest from background: This step consists of thresholding

each image (frame) of the video (x, y, t) to segment the zones of interest (remove noise and atypical values). Our strategy includes performing an automatic selection of threshold value for each Gaussian blurred image (I_G) (σ = 3.5 µm) considering the mean value (M_I) and the standard deviation (S_I) of the image I_G. The threshold value is defined by: $T_I = M_I + 6S_I$.

2. Compute the connected components: The connected components labeling is used to detect connected regions in the image (a digital continuous path exists between all pairs of points in the same component - the sperm heads). This heuristic consists of visiting each pixel of the image and creating exterior boundaries using pixel neighbors, accordingly to a specific type of connectivity.
3. Measure sperm head fluorescence. For each region of interest, identify the centroid in the fluorescence channel (sperm head) and measure the mean value.
4. Compute the relative positions of the sperm heads within the imaging field, and assign them to either R1, R2, R3 or R4 concentric regions around the centroid of the UV flash intensity distribution. The radii of R1, R2, R3 or R4, were 25, 50, 75 and 100 µm, respectively.
5. Repeat steps 1 to 4 in a frame-wise basis.

Step 1 of the algorithm filters out shot noise and atypical values; step 2 divides the images in N connected components on the location of the sperm heads; step 3 quantitates sperm head fluorescence, and finally step 4 computes the relative sperm position on the imaging field. A similar approach has been recently used to identify replication centers of adenoviruses in fluorescence microscopy images (Garces et al., 2016).

We automatically analyzed up to 267 videos of *S. purpuratus* spermatozoa, each containing tens of swimming cells, exposed to five distinct speract concentration

gradients.

Computing the dynamics of speract concentration gradients

The dynamics of the chemoattractant gradient was computed using the Green's function of the diffusion equation:

$$c(r,t) = \frac{C_0}{\sqrt{2\pi\sigma}} e^{-r^2/2\sigma^2} + C_b \quad (5)$$

This equation for the concentration tells us that the profile has the form of a Gaussian. The width of the Gaussian is $\sigma = \sqrt{4D(t+t_0)}$, and hence it increases as the square root of the time. C_b is the basal concentration of the chemoattractant, D is the molecular diffusivity.

The speract concentration gradients were generated via the photolysis of 10 nM caged speract (CS) with a 200 ms UV pulse delivered through each of four different optical fibers with internal diameters of 200 µm, 600 µm, 2 mm and 4 mm (at two different positions). Light intensity was normalized dividing each point by the sum of all points of light intensity for each fiber and multiplying it by the fiber potency (measured at the back focal plane of the objective) in miliwatts (mW) (**Figure 2 - table supplement 1**). Each spatial distribution of instantaneously-generated speract concentration gradient was computed by fitting their corresponding normalized spatial distribution of UV light (Residual standard error: 2.738 x 10^{-5} on 97 degrees of freedom), considering an uncaging efficiency of 5%, as reported (Tatsu et al., 2002).

The diffusion coefficient of a molecule is related to its size by the Stokes-Einstein equation:

$$D = \frac{kT}{6\pi\eta R_h} \quad (6)$$

where k is Boltzmann's constant, T is the temperature, η is the viscosity of the solvent, and R_h is the hydrodynamic radius (Lakowicz, 2006). The hydrodynamic radius

R_h of speract was calculated by modeling the molecules in terms of equivalent hydrodynamic spheres.

$$R_h = \left(\frac{3M\bar{v}}{4\pi}\right)^{1/3} \quad (7)$$

where M is the molecular weight, and $\bar{v}$ is the specific gravity (Lakowicz, 2006). The volume of an equivalent spherical particle is $V_e = 4/3\,\pi R_h^3$. Equations **6** and **7** show that the radius and diffusion coefficient are weakly dependent on the molecular weight.

The diffusion coefficient of speract has not been measured experimental, nonetheless it can be estimated following equations 6 and 7. The diffusion coefficient of a similar chemoattractant molecule, resact (with fourteen amino acids), has been reported, D_{resact} = 239 ± 7 μm^2 s^{-1} (Kashikar et al., 2012). If we consider that speract is a decapeptide, the 1.4 fold difference in molecular weight between speract and resact would imply a $(1.4)^{1/3}$ fold difference in their diffusion coefficients, which is close to the experimental error reported (Kashikar et al., 2012). For the sake of simplicity, the spatio-temporal dynamics of the distinct instantaneously generated speract gradients was modeled considering a speract diffusion coefficient of $D_{speract}$ = 240 μm^2 s^{-1}.

The hydrodynamic radius of speract (R_h = 8.8 Å) was computed with equation (**6**), with $D_{speract}$ = 240 μm^2 s^{-1}, k = 1.38 x 10^{-23} J K^{-1}, T = 288.15 K and η = 0.001 N s /m^2.

Computing $[Ca^{2+}]_i$ dynamics, chemotactic behavior, and the stimulus function of single spermatozoa

Spermatozoa were tracked semi-automatically by following the head centroid with the MtrackJ plugin (Meijering et al., 2012) of ImageJ 1.49u. Single cell $[Ca^{2+}]_i$ signals were computed from the mean value of a 5 x 5 pixels region, centered at each sperm head along the time.

Chemotactic behavior was quantified using the linear equation chemotaxis index (*LECI*) employing different temporal windows before (control) and after uncaging

speract. *LECI* is defined as the negative value of the slope (*LECI* = -*l*) of a least square linear regression $r(t) = lt + r_0$ (Yoshida et al., 2002) where $r(t)$ is the sperm head distance to the center of the speract concentration gradient, t is the time after UV pulse measured in seconds, with $t \in [0 - 3; 3.2 - 6.2; 6.2 - 9.2]$ seconds. Positive *LECI* indicate movement towards the chemoattractant source. The center of the speract gradient was identified as the centroid of the UV flash intensity distribution.

The head position of each spermatozoa was used to compute the local concentration of speract at $r(x, y)$ over each frame. The stimulus function of single spermatozoa $s = c(r, t)$ was computed by solving equation (**5**), considering both their swimming trajectories, and the spatio-temporal evolution of a given speract concentration gradient. The profiles of UV light were used to compute the initial conditions at $c(r, t_o)$.

The phase- and temporal-shifts between time derivative of the stimulus function ds/dt and the internal Ca^{2+} oscillator triggered by speract, were computed from their normalized cross-correlation function.

Analysis of speract induced Ca^{2+} transients with immobilized spermatozoa.

Imaging chambers were prepared by coating cover slips with 50 µg/ml poly-D-lysine, shaking off excess, and allowing to air-dry. Coated cover slips were then attached to imaging chambers. Fluo-4 labeled spermatozoa were diluted 1:40 in ASW, immediately placed into the chambers, and left for 2 min, after which unattached sperm were removed by washing with ASW. The chambers were then filled with 0.5 ml of ASW containing 500 nM of caged speract, and mounted in a TC-202 Bipolar temperature controller (Medical Systems Corp.). Images were collected with Andor iQ 1.7 software (Andor Bioimaging, NC) at 90 fps in full-chip mode, binning 4x4 (observation field of 200 µm x 200 µm). The imaging setup was the same as that used for swimming spermatozoa. The caged speract was photo-released with a 200 ms UV

650 pulse delivered through an optical fiber (4 mm internal diameter) coupled to a Xenon
651 UV lamp (UVICO, Rapp Opto Electronic). The optical fiber was mounted on a
652 "defocused" configuration to minimized the generation of UV light heterogeneities.
653 Images were processed off-line using ImageJ 1.4.5s. Overlapping spermatozoa and
654 any incompletely adhered cells, which moved during the experiment, were ignored.
655 Fluorescence measurements in individual sperm were made by manually drawing a
656 region of interest around the flagella with the line tool of ImageJ.
657 Programs were written in R statistical software.
658
659 **Theory**
660 *Constraints over the detection of chemoattractant concentration fields.*
661 Strategies for chemoattractant sampling based on local concentration gradients require
662 the concentration to be high enough to ensure that the measured average difference at
663 two nearby locations is larger than typical fluctuations (Wood et al., 2015). As
664 stochastic fluctuations limits the precision with which a microorganism can, in a given
665 time *T*, determine the concentration of a surrounding chemoattractant (Berg and Purcell,
666 1977, Vergassola et al., 2007), the rate of encounter between a chemoattractant *c*
667 diffusing with effective diffusivity *D* and its receptor, with a binding site of effective
668 radius *s*, is given by:
669 $$J(\boldsymbol{r}) = 4\pi sDc(\boldsymbol{r}) \quad (8)$$
670 For reliable assessment of the local concentration *c(r)*, a spermatozoon provided with
671 N_R number of chemoattractant receptors, collects detection events over time T_{int}. The
672 average number of detection events will then be $J(r)N_R T_{int}$. Typical stochastic
673 fluctuations are of the order of the square root of the mean (Berg and Purcell, 1977).
674 Then the condition for the signal to emerge from the noise reads:

675 $$\sqrt{N_R s D c T_{int}} \ll 1 \quad (9)$$

676 Then, it follows that the spermatozoon will experience an uncertainty $u_1 =$
677 $(N_R s D c T_{int})^{-1/2}$ (**eq. (1)**), for measuring a variation on the local concentration of
678 chemoattractant (**Figure 1 - figure supplement 1**).

679

680 To reliably measure a concentration gradient of chemoattractant, the difference in
681 counts collected by the spermatozoon in the interval measurement must be above the
682 noise level (**Figure 1a**). The corresponding conditions can be stated as (Berg and
683 Purcell, 1977, Vergassola et al., 2007):

684 $$\left(v T_{int} \frac{dc}{dr}\right) N_R s D T_{int} \gg \sqrt{N_R s D c T_{int}} \quad (10)$$

685 $$v T_{int} \frac{d \log c}{dr} \ll 1 \quad (11)$$

686 Here, v is the swimming velocity and dc/dr is the concentration gradient of the
687 chemoattractant. The first inequality indicates that the signal-to-noise ratio for the
688 difference in the number of hits experienced by the swimming spermatozoon across the
689 integration time T_{int} be larger than unity. The second inequality is the requirement of
690 locality, *i.e.* the change in concentration across the distance spanned during T_{int} needs
691 to be small compared to the local concentration itself.

692 The information to determine the direction of the chemoattractant gradient results
693 from the magnitude difference of the signal at two sampled positions. Then the
694 condition for the signal to emerge from the noise on a chemoattractant field reads:

695 $$v^{-1} T^{-3/2} (N_R s D)^{-1/2} c^{1/2} \varepsilon^{-1} \ll 1 \quad (12)$$

696 where $\varepsilon = dc/dr$ is the chemoattractant concentration gradient. Then, it follows that
697 the least fractional error of the chemoattractant gradient direction due to the state of
698 occupation of receptors is $u_2 = v^{-1} T^{-3/2} (N_R s D)^{-1/2} c^{1/2} \varepsilon^{-1}$ (**Figure 1, eq. (2)**).

699 Assuming an exponentially decaying concentration, reliable integration time T_{int}
700 scales as $exp(r/3\lambda)$ (Vergassola et al., 2007).

701 *Statistical analyses*

702 Data are presented for individual spermatozoa (n) collected from up to three sea
703 urchins. All statistical tests were performed using R software (R Core Team, 2016). The
704 significance level was set at 95%.

705

706 **Acknowledgements**

707 The authors thank Dr. Tatsu Yoshiro for providing the caged speract, and Drs.
708 Hermes Gadêlha, David Smith and Nina Pastor for stimulating discussions and a critical
709 reading of the manuscript. AG thanks Dr. Manabu Yoshida and Dr. Kaoru Yoshida for
710 feedback about sperm chemotaxis in marine invertebrates, and to the Japan Society for
711 the Promotion of Science (JSPS invitation fellowship for research in Japan to A.G.,
712 short term JSPS/236, ID no. S16172).

713

714 **Author contributions**

715 A.G., A.D. and I.T. conceived the project; A.G. and V.J.S. performed the
716 experiments; H.R.G., A.G., I.T., V.J.S. and M.V. analyzed the data; A.G., I.T. and
717 H.R.G performed the mathematical model calculations and wrote the corresponding
718 section; A.D., A.G., H.R.G. and I.T. participated in the design and drafting of the
719 manuscript J.C., C.D.W. and C.B. provide feedback for conceptualization and drafting
720 of the manuscript. All authors approved the final version of the article.

721

722 **Competing interests**

723 The authors declared that no competing interests exist.

724

725 **Funding**

726 A.D. and A.G. acknowledges grants from the Consejo Nacional de Ciencia y
727 Tecnología (CONACyT Fronteras 71, CONACyT Ciencia Básica 252213), A.G., A.D.
728 and C.B to Programa de Apoyo a Proyectos de Investigación e Innovación Tecnológica
729 UNAM (PAPIIT/DGAPA) (IA202417, IN205516, IN206016 and IN112514
730 respectively). We acknowledge CONACYT and PAPIIT for fellowships to M.V.P.; the
731 Spanish Ministry of Economy and Competitiveness Grants No. FIS2013-48444-C2-1-P,
732 FIS2016-77692-C2-1- P, the Subprogram Ramón-y-Cajal and the Ibero-America
733 Program-Santander Universities 2015 (I.T.).

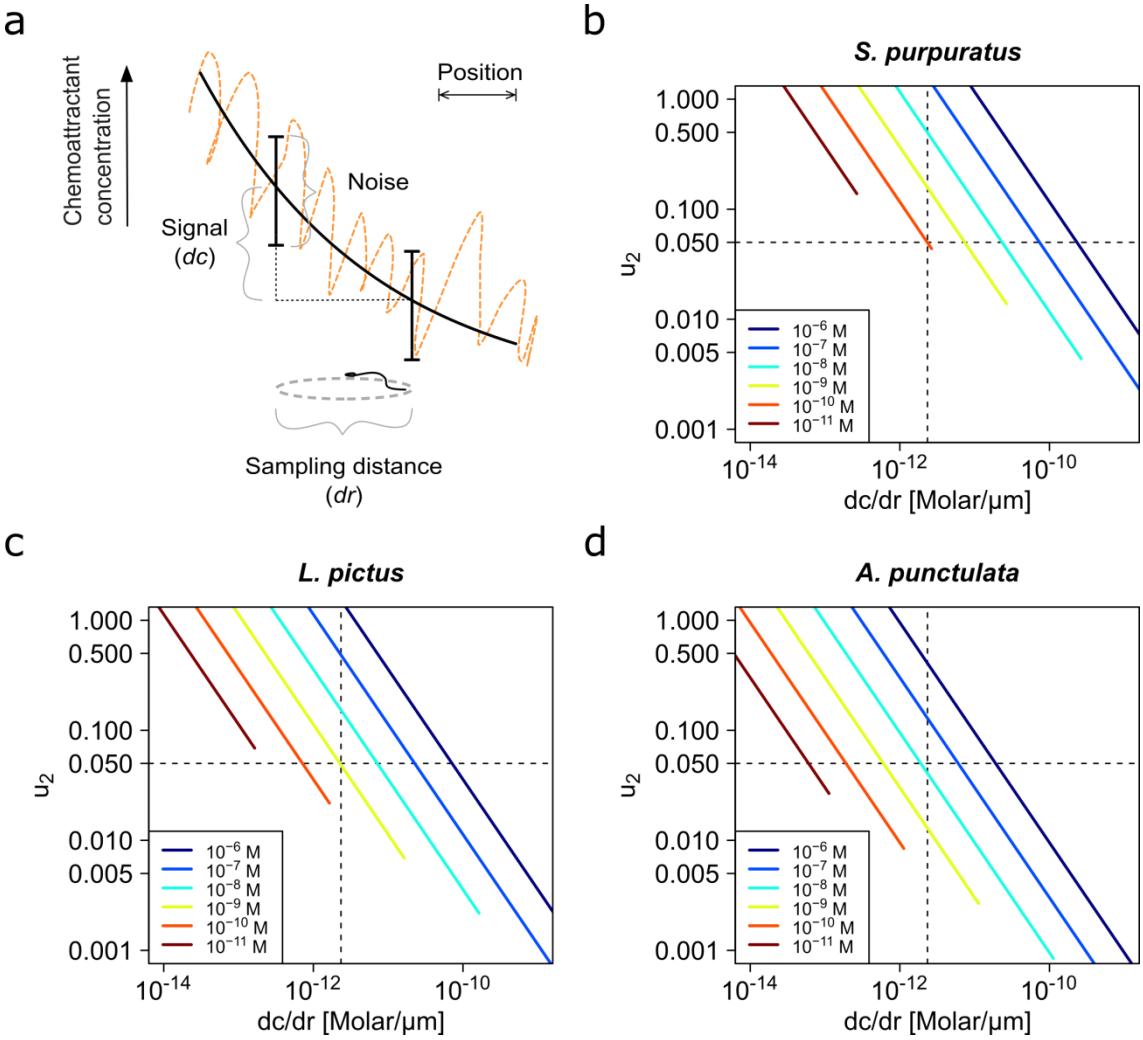

Figure 1. Physics of chemoreception. **a**. Determining the direction of the chemoattractant gradient requires that the signal difference *dc* between two sampled positions *dr* must be greater than the noise. **b-d.** The uncertainty in the determination of the chemoattractant gradient direction, u_2, plotted against the slope of the gradient, *dc/dr*, in log-log scale, for different chemoattractant concentrations, **(b)** *S. purpuratus*, **(c)** *L. pictus*, and **(d)** *A. punctulata* spermatozoa (See **Figure 1 - table supplement 1** for the list of parameter values taken in consideration for panels **b-d**).

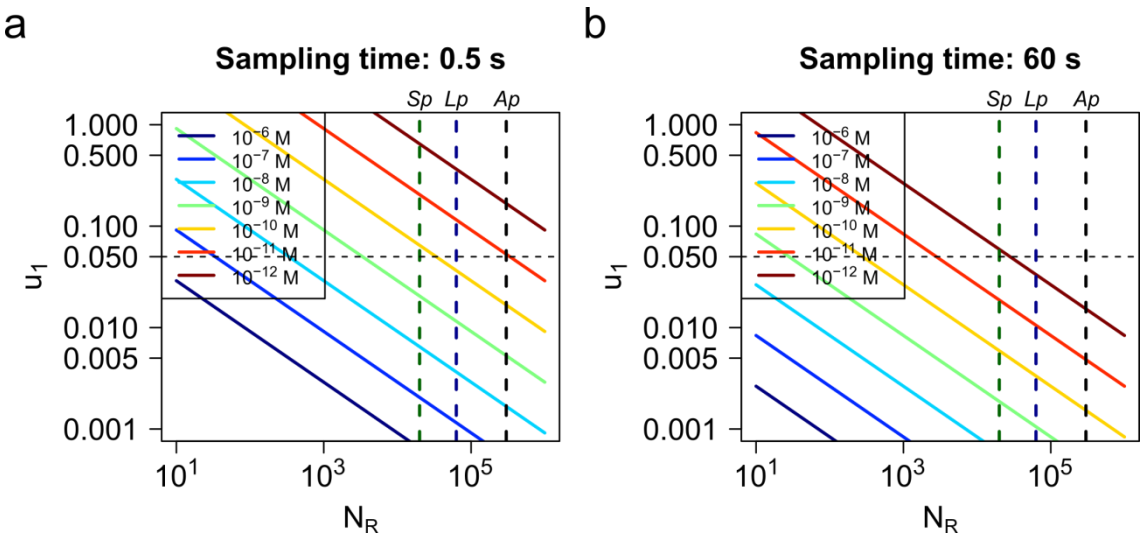

Figure 1 - figure supplement 1. Uncertainty for the detection of a homogeneous chemoattractant concentration field. The uncertainty for determining the chemoattractant concentration u_1 versus the receptor number N_R for different concentrations (10^{-6} to 10^{-12} M), for a sampling interval of T = 0.5 s **(a)**, or a T = 60 s **(b)**. Vertical lines indicate the number of receptors of Sp = *S. purpuratus* (dark green), Lp = *L. pictus* (dark blue) and Ap = *A. punctulata* (black) spermatozoa. Parameters: sampling interval T = 0.5 s **(a)** and 60 s **(b)**, speract diffusion coefficient D = 239 µm^{2}s^{-1}, hydrodynamic radius of speract (as proxy of receptor pocket size) R_h = 0.79 nm (see **figure 1 - figure supplement 2 and figure 1 - table supplement 1**).

Spermatozoan species	***S. purpuratus***	***L. pictus***	***A. punctulata***
N_R **[per cell]**	2 x 10^{4b}	6.3 x 10^{4b}	3 x 10^{5}
D **[cm^2s^{-1}]**	2.4 x 10^{-6c}	2.4 x 10^{-6c}	2.4 x 10^{-6c}
s **[cm]**	1.65 x 10^{-7c}	1.65 x 10^{-7c}	1.65 x 10^{-7c}
T **[s]**	0.39 ± 0.08[a]	0.52 ± 0.22[a]	0.6
v **[cms^{-1}]**	121 ± 13 x 10^{-4a}	144 ± 36 x 10^{-4a}	200 x 10^{-4}
dr **[cm]**	28 ± 6 x 10^{-4a}	46 ± 14 x 10^{-4a}	60 x 10^{-4}

Figure 1 - table supplement 1. Parameters of the chemoattractant sampling model for each species. Note that the main differences between species are the number of receptors N_R and the velocity v of the spermatozoon. D diffusion coefficient; s hydrodynamic radius of speract (as proxy of chemoattractant receptor's pocket radius); T sampling time (time to swim half circumference in the boundary close to the water-glass interface); dr = sampling interval (circumference diameter). [a]Measured in this study (mean ± sd; N = 3 sea urchins; n = 495 (*S. purpuratus*), 56 (*L. pictus*) spermatozoa. [b](Nishigaki et al., 2001, Nishigaki and Darszon, 2000). [c]Calculated in this study (see section: ***Computing the dynamics of speract concentration gradients*** in **Materials and Methods**, and **Figure 1 - figure supplement 2**).

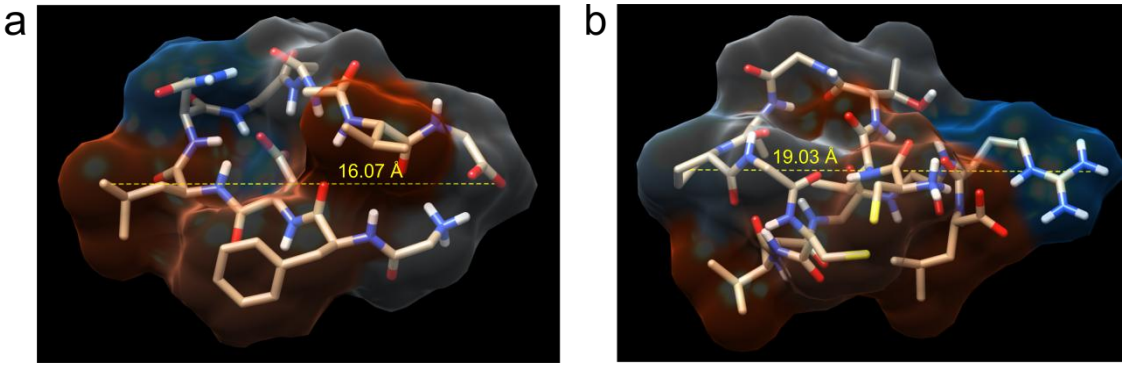

Figure 1 - figure supplement 2. Speract and resact modeling. Five speract and resact structures, respectively, were modeled using PEP-FOLD (Maupetit et al., 2009, Thevenet et al., 2012, Maupetit et al., 2010), and used to estimate an equivalent hydrodynamic radius by computing the length of the mayor axis of each model: **a.** Speract (16.18 ± 0.41 Å). **b.** Resact (18.97 ± 1.79 Å). The estimates of the mayor axis of the speract model were similar to their corresponding hydrodynamic diameter estimates ($d = 2R_h = 2(8)$ Å = 1.6 nm) computed with the Stokes-Einstein equation (R_h = 0.88 nm) (see section: *Computing the dynamics of speract concentration gradients* in **Materials and Methods**). Models were visualized with chimera 1.11.2 (Pettersen et al., 2004).

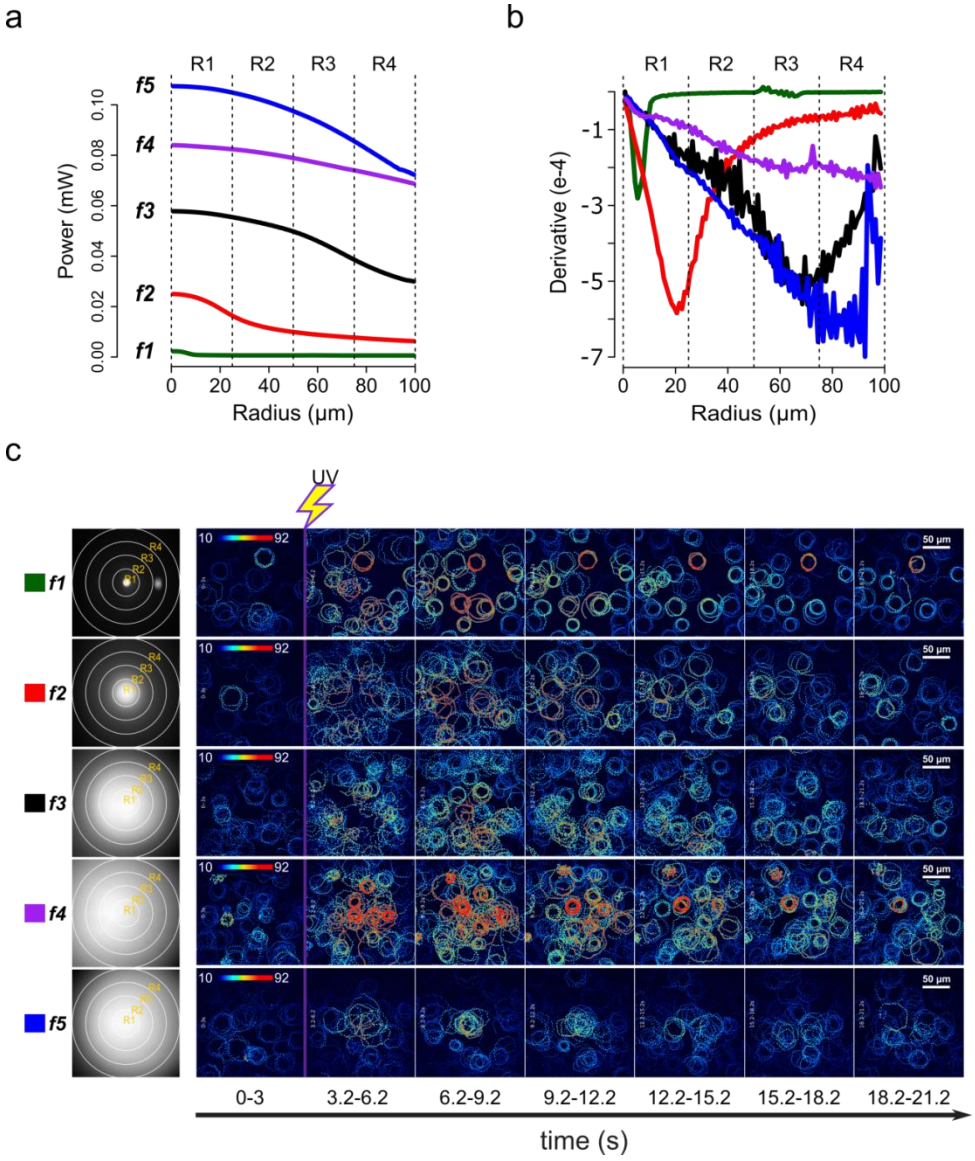

Figure 2. Screening of speract concentration gradients. a. Radial profile of the UV light scattered at the glass-liquid interface for each optical fiber (*f1-f5*). **b**. Derivatives of radial distribution for each optical fiber. **c**. Spatial distribution of the UV flash energy (left), and typical motility and $[Ca^{2+}]_i$ responses of spermatozoa exposed to different concentration gradients of speract (right). F-F_0 time projections, showing spermatozoa head fluorescence each 3 s before and after 200 ms UV photoactivation of 10 nM caged speract in artificial sea water. The pseudo-color scale represents the relative fluorescence of fluo-4, a Ca^{2+} indicator, showing maximum (red) and minimum (blue) relative $[Ca^{2+}]_i$. Scale bars of 50 µm.

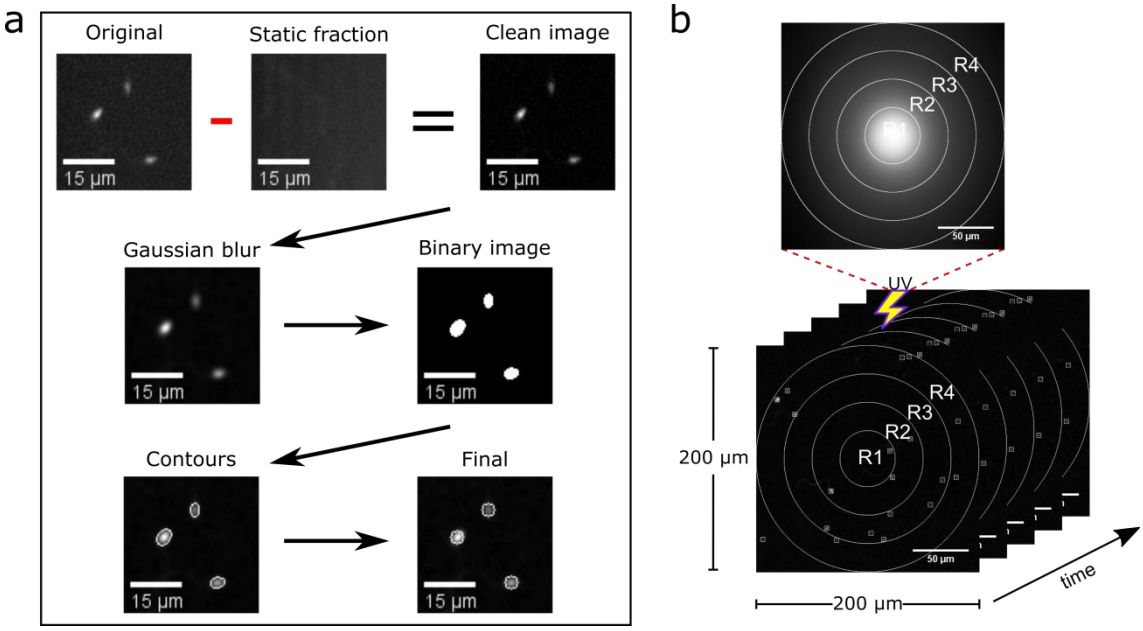

Figure 2 - figure supplement 1. Automatic segmentation of swimming spermatozoa. a. Working-flow of the algorithm: Video microscopy images were background subtracted by removing the temporal average intensity projection (static fraction) of the first un-stimulated frames (93 frames = 3 seconds) from the whole video (25 seconds). The resulting images were convolved with a low-pass spatial frequency filter to eliminate typical detector shot-noise. The resulting images were thresholded to generate arrays of regions of interest (ROIs), a heuristic search for connected components is then applied to label single ROIs and to assign the corresponding pixels to unique spermatozoa. Scale bar of 15 µm. **b.** The positions of the sperm heads within the imaging field are assigned to either R1, R2, R3 or R4 concentric regions around the centroid of the UV flash intensity distribution. Each ROI was also used to compute the sperm head fluorescence from the raw video microscopy images (as the mean value of the ROI). Scale bar of 50 µm.

799

	Physical diameter (mm)	UV power at the back focal plane of the objective (mW)*
f1	0.2	0.07
f2	0.6	1.25
f3	2	4.7
f4	4	7.8
f5	4	9.46

800

801 **Figure 2 - table supplement 1. Physical diameter of the optical fibers, and UV light**

802 **power measured at the back focal plane of a 40×/1.3NA oil-immersion objective.**

803 *Typically, there is a 20% loss of light power due to scattering within the optics.

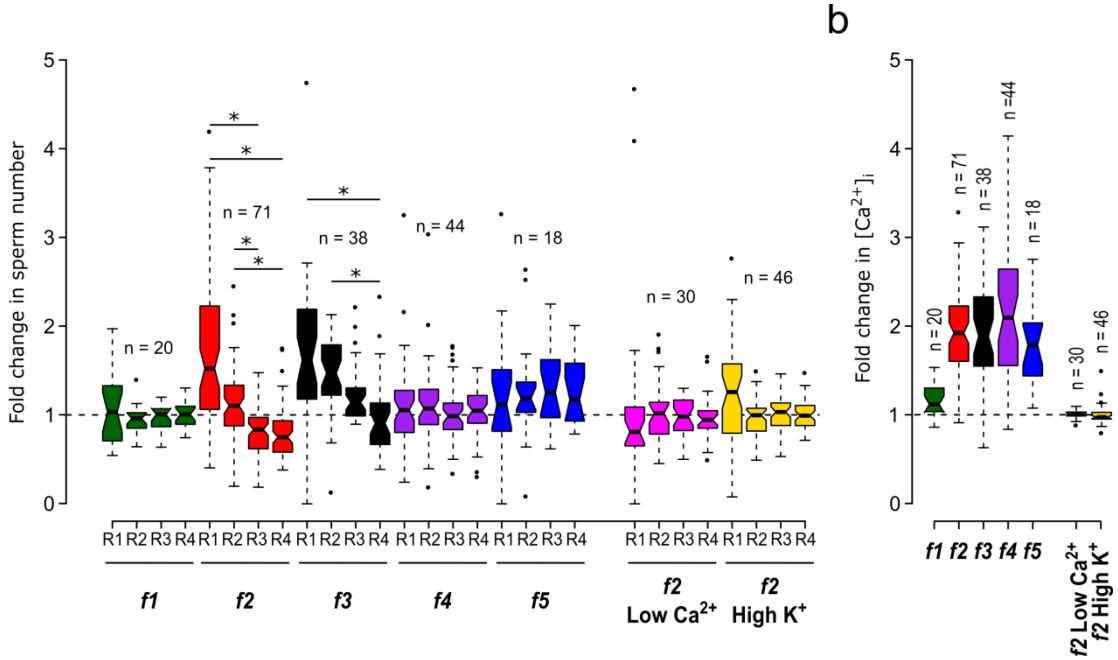

Figure 3. Motility and $[Ca^{2+}]_i$ responses of *S. purpuratus* spermatozoa exposed to specific concentration gradients of speract. a. Fold change in sperm number, defined as the number of spermatozoa at the peak of the response (6 s) relative to the mean number before speract stimulation (0-3 s) (see **figure 3 - figure supplement 1**). **b**. Relative changes in $[Ca^{2+}]_i$ experienced by spermatozoa at the peak response (6 s) after speract stimulation. Negative controls for spermatozoa chemotaxis are artificial sea water with nominal Ca^{2+} (Low Ca^{2+}); and artificial sea water with 40 mM of K^+ (High K^+). Both experimental conditions prevent chemotactic responses by inhibiting the Ca^{2+} membrane permeability alterations triggered by speract; the former disrupts the Ca^{2+} electrochemical gradient, and the later disrupt the K^+ electrochemical gradient required as electromotive force needed for the opening of Ca^{2+} channels. Number of experiments (n) on the top of each experimental condition. Each box contains 50% of single events, the inner lines indicate the median and the error bars delimit the 95% outliers. The notch display a confidence interval around the median (median +/- 1.57 x $IQRn^{-1/2}$). If two boxes notches do not overlap, there is evidence that their medians differ (95% confidence). *Statistical significance, $p < 0.05$; Multiple comparison test after Kruskal-

821 Wallis. Studies at the population level are presented in **figure 3 - figure supplement 1**,
822 while studies considering the absolute number of spermatozoa at two periods: 3s and 6s
823 (3 seconds before and after speract exposure, respectively) are presented in **figure 3 -**
824 **figure supplement 2**.
825

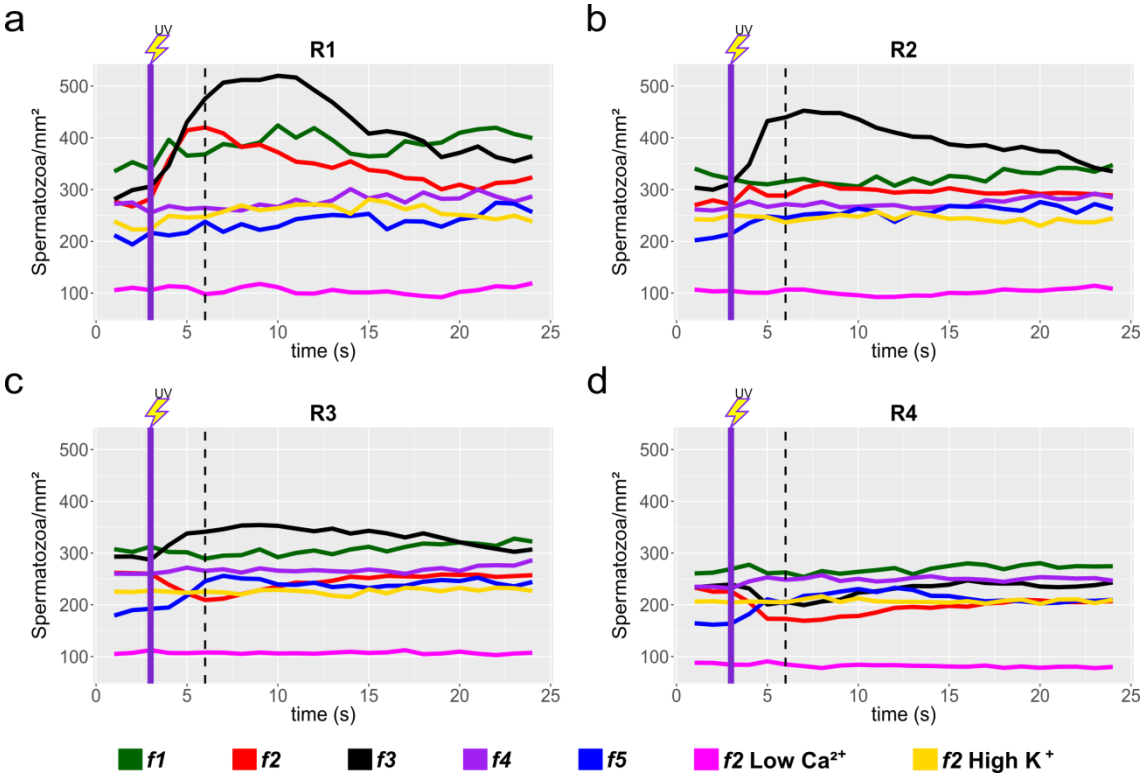

Figure 3 - figure supplement 1. Sperm response to speract photo-release, collated data from individual experiments. Sperm motility responses to different speract concentration gradients (*f1*, *f2*, *f3*, *f4*, *f5*) at R1 (**a**), R2 (**b**), R3 (**c**) and R4 (**d**) concentric regions. Negative controls for sperm chemotaxis are artificial sea water with nominal 0 Ca^{2+} (Low Ca^{2+}); and artificial sea water with 40 mM of K^{+} (High K^{+}). Each time trace, represent the mean sperm density from up to 20 video microscopy experiments (raw data distributions at two periods 3s and 6s are presented in **figure 3 - figure supplement 2**). Note that peak responses occurred at second 6, three seconds after speract exposure (indicated as vertical dotted lines).

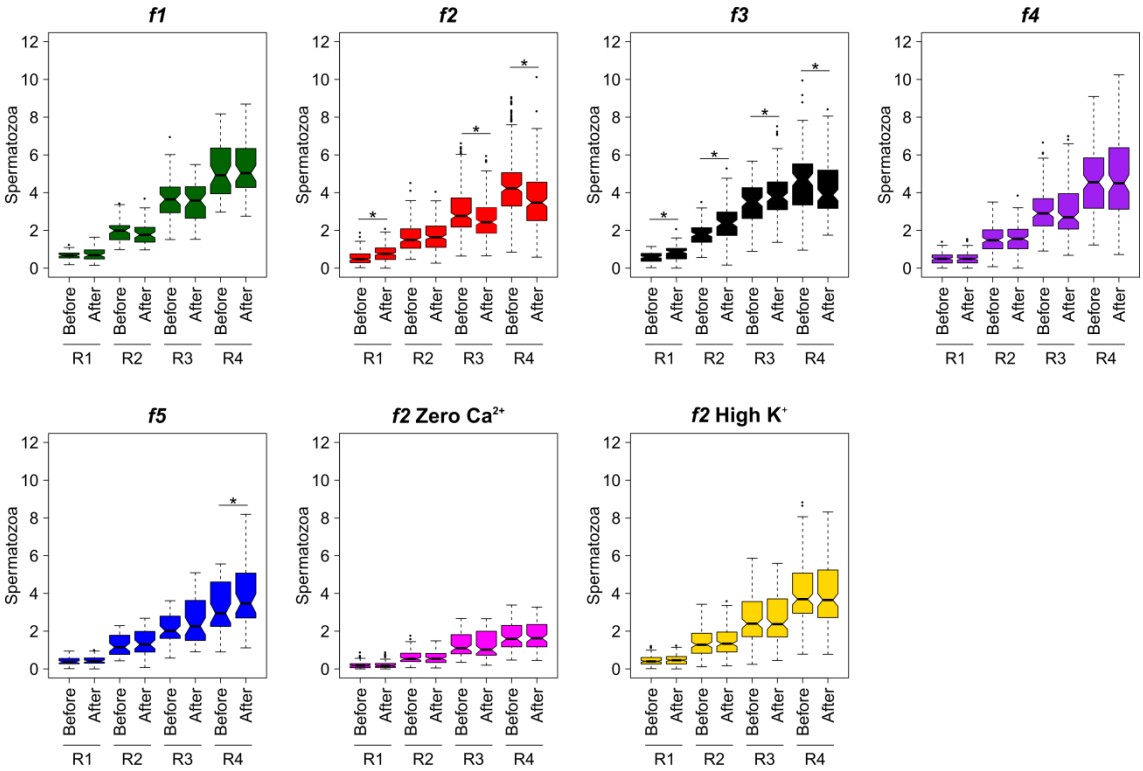

Figure 3 - figure supplement 2. Absolute number of sperm cells, three seconds before and three seconds after speract photo-release through either *f1*, *f2*, *f3*, *f4*, *f5* optical fibers. Absolute number of spermatozoa scored at either R1, R2, R3 or R4 concentric regions around the centroid of the UV flash intensity distribution. Each box contains 50% of single events, the inner lines indicate the median and the error bars delimit the 95% outliers. *Statistical significance, $p < 0.05$; Mann-Whitney test.

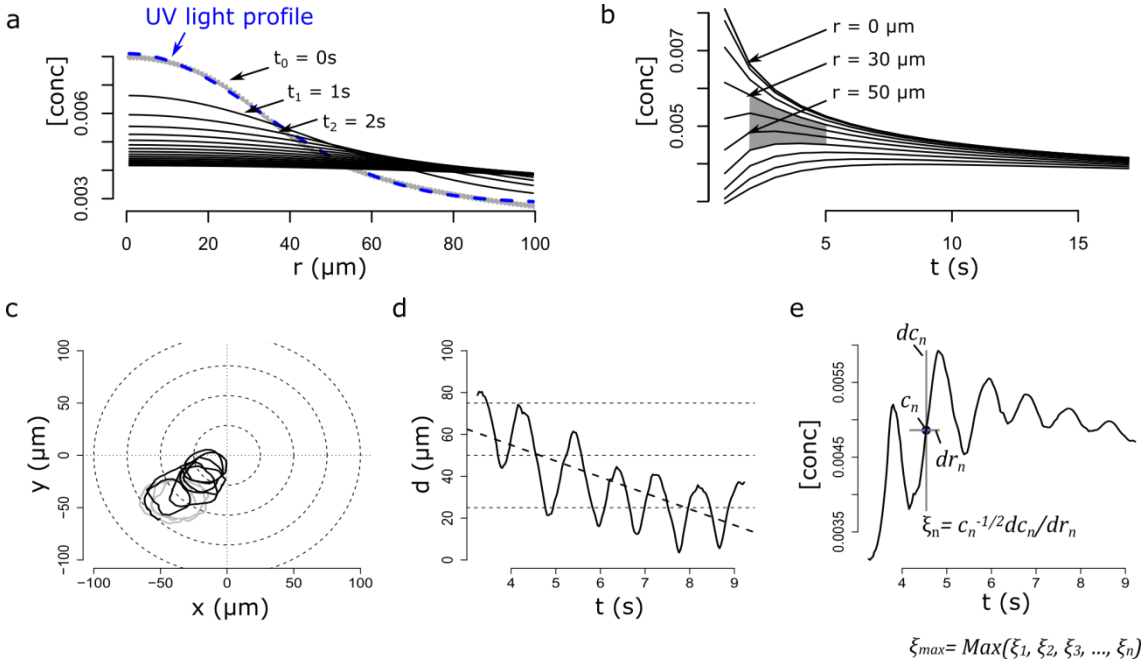

844

845 **Figure 4. Steep speract gradients attract *S. purpuratus* spermatozoa. a.** Dynamics
846 of the *f2* speract gradient. The blue dashed line (t_0 = 0 s) corresponds to a Gaussian
847 distribution fitted to the UV light profile, and illustrates the putative shape of the
848 instantaneously-generated speract concentration gradient. Solid black lines illustrate the
849 temporal evolution of the speract concentration field after t = 1, 2, 3, …, 20 seconds. **b.**
850 Temporal changes in *f2* speract field computed radially (each 10 μm) from the center of
851 the gradient. A region where the concentration of speract barely changes is shown in
852 gray. **c.** Characteristic motility changes of a *S. purpuratus* spermatozoon exposed to the
853 *f2* speract gradient. Solid lines illustrate its swimming trajectory 3 s before (gray) and 6
854 s after (black) speract exposure. **d**. Spermatozoon head distance to the source of the
855 speract gradient versus time, calculated from black trajectory in **c**. LECI index is
856 computed from the least squared linear regression of the head distance to the source, a
857 negative slope (as shown) indicates chemotaxis (positive LECI). **e**. Stimulus function
858 computed from the swimming behavior of the spermatozoon in **c**, considering the
859 dynamics of **a**.

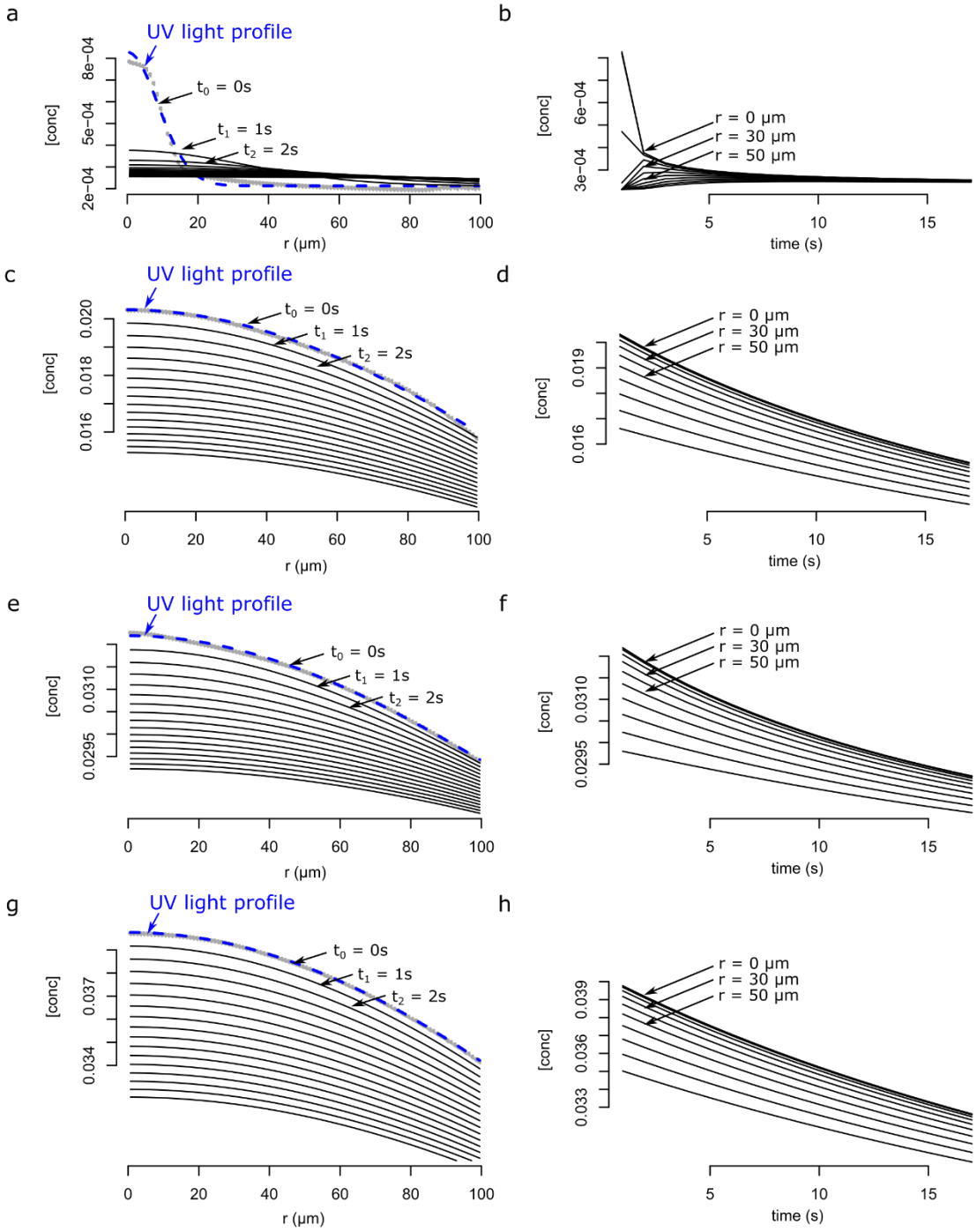

Figure 4 - figure supplement 1. Modeling of the dynamics of speract gradient based on the UV light profile of distinct optical fibers. The radial profiles of the UV light scattered at the glass-liquid interface of *f1*, *f3*, *f4*, *f5* optical fibers are shown in gray. The speract gradient was generated as in **figure 4**, but with the corresponding *f1* (**a**), *f3* (**c**), *f4* (**e**) and *f5* (**g**) optical fibers. *Left panels* - The dynamics of the speract gradient computed as is in **figure 4**. The blue dashed line (t_0 = 0) corresponds to a

867 Gaussian distribution fitted to the UV light profile, and illustrates the putative shape of
868 the instantaneously generated speract gradient. Solid black lines illustrate the shape of
869 the speract gradient after t = 1, 2, 3, …, 20 seconds. *Right panels* - Simulated temporal
870 changes in speract concentration gradients of *f1* (**a**), *f3* (**c**), *f4* (**e**) and *f5* (**g**) at each 10
871 radial µm point from the center of the concentration gradient.

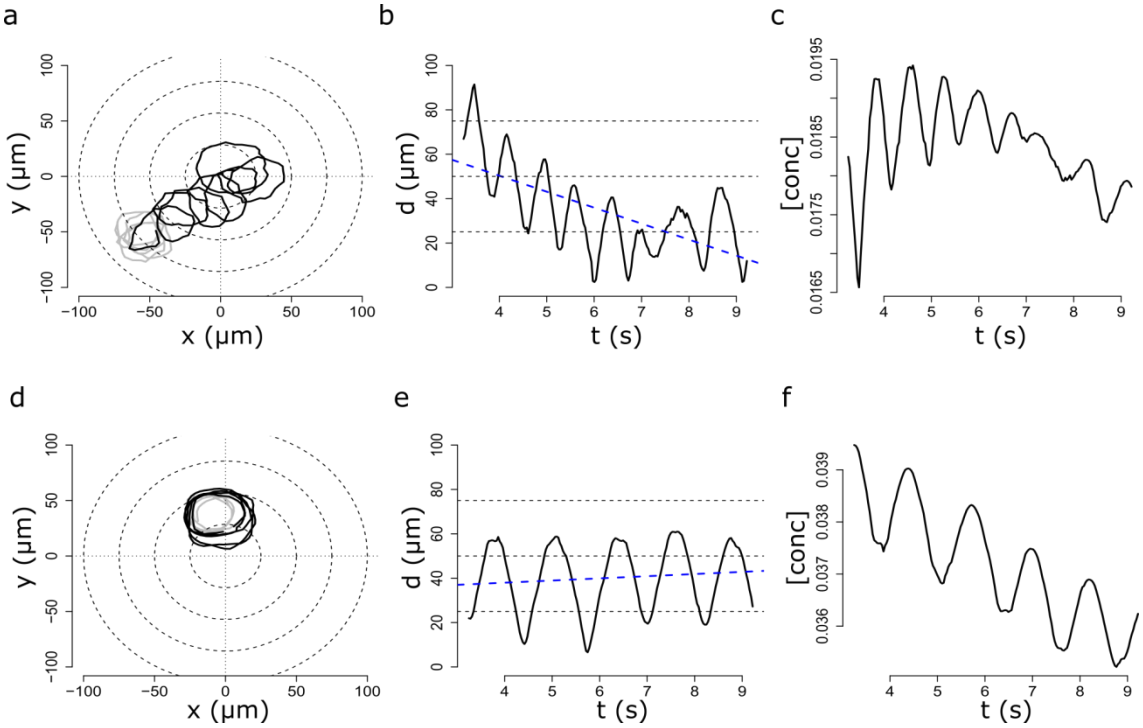

Figure 4 - figure supplement 2. Characteristic motility changes of a *S. purpuratus* spermatozoon exposed to *f3 and f4* speract gradients (chemotactic vs non-chemotactic response). Panels **a**, **b** and **c** show single cell responses to the *f3* speract gradient (chemotactic); and panels **d**, **e** and **f** to the *f4* speract gradient (non-chemotactic). **a, d.** Solid lines illustrate the spermatozoon swimming trajectory 3 s before (gray) and 6 s after (black) speract gradient exposure. **b, e**. Spermatozoon head distance to the source of the speract gradient versus time calculated from **a** and **d**, respectively. **b, e**. Stimulus function computed from **a** and **d**, considering the spatio-temporal dynamics of speract computed for the *f3* and *f4* gradients, respectively.

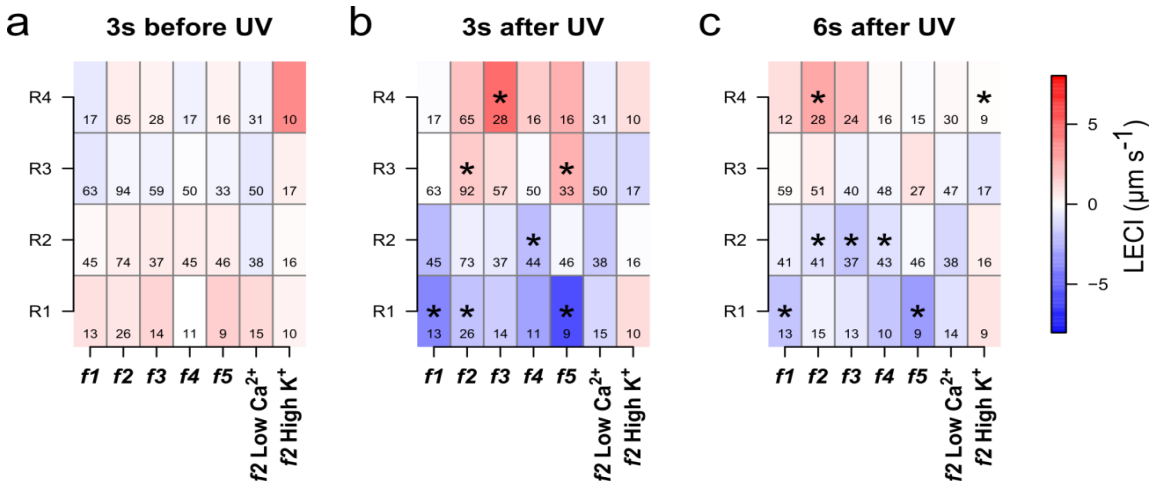

Figure 5. *S. purpuratus* spermatozoa selectively experience chemotaxis towards speract gradients. Chemotactic behavior quantified using the linear equation chemotaxis index (*LECI*) before (**a**), as control experiment, and after exposure to either *f1*, *f2*, *f3*, *f4* or *f5* speract gradients (**b**, **c**). The color scale indicates the mean *LECI* value calculated from tens of *S. purpuratus* spermatozoa located in either R1, R2, R3, or R4 regions prior speract photo-release (3 s after UV light irradiation (**b**), or 6 s after UV light exposure (**c**)). Positive LECIs (shown in red) indicate movement towards the chemoattractant source. Note that spermatozoa that were in R3 and R4 distal regions prior speract gradient exposure experience chemotaxis only in response to *f2*, *f3*, and *f5* speract gradients (**b**, **c**). Numerals indicate the number of spermatozoa analyzed in each experimental condition. *Statistical significance, $p < 0.05$; Student's t-test.

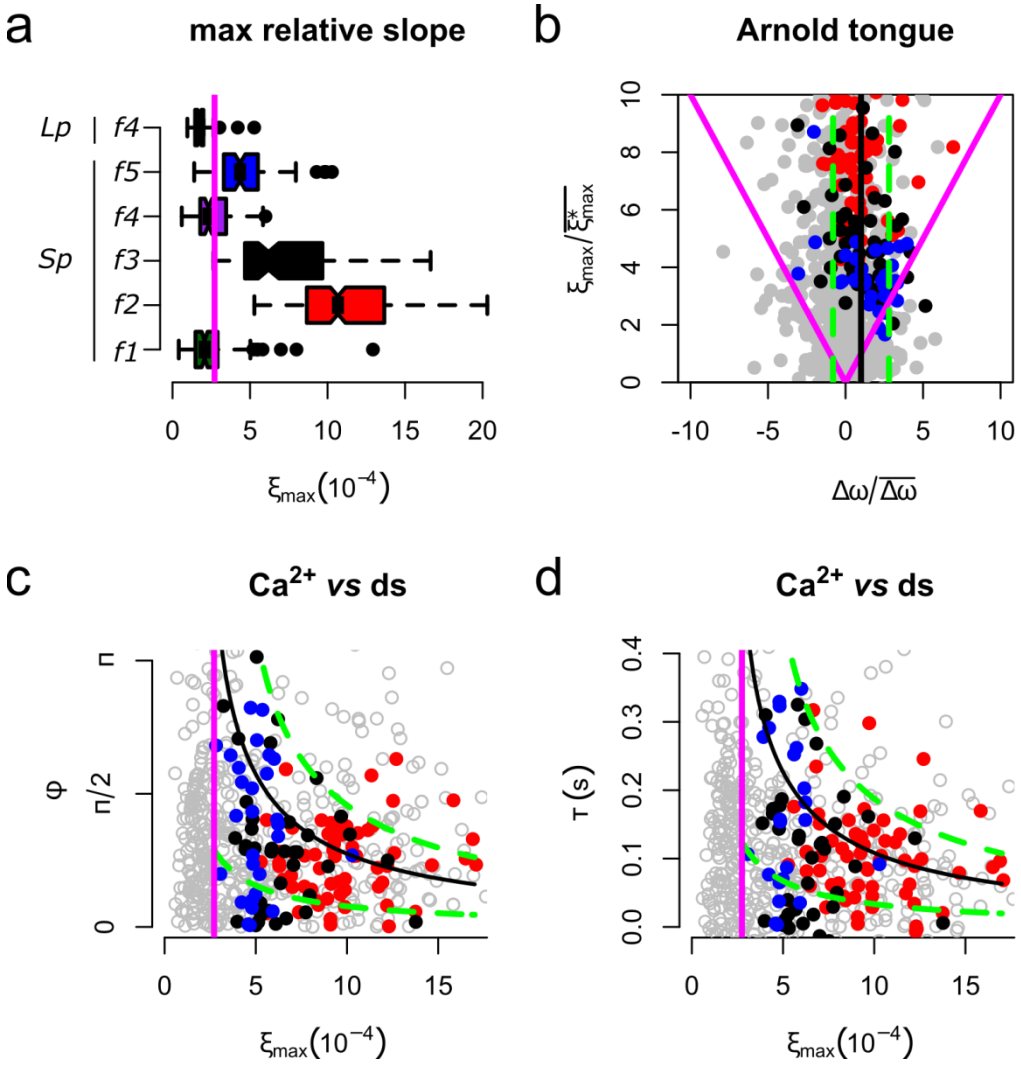

Figure 6. The slope of the speract gradient generates a frequency-locking phenomenon between the stimulus function and the internal Ca^{2+} oscillator triaggered by speract. a. Maximum relative slopes (ξ_{max}) experienced by *S. purpuratus* (Sp) when exposed to *f1, f2, f3, f4, f5* speract gradients. The maximum relative slopes experienced by *L. pictus* spermatozoa (Lp) towards *f4* experimental regime are also shown. Note that ξ_{max} for *f2*, *f3*, and *f5*, are up to 2-3 times greater than in *f4*, regardless of the species. **b.** Arnold's tongue indicating the difference in intrinsic frequency of the internal Ca^{2+} oscillator of *S. purpuratus* spermatozoa, just before and after the speract gradient exposure. **c**. Phase difference between the time derivative of the stimulus function and the internal Ca^{2+} oscillator of *S. purpuratus* spermatozoa, obtained by computing the cross-correlation function between both time series (**Figure 6 - figure**

908 **supplement 2**). **d**. Phase difference between the time derivative of the stimulus function
909 and the internal Ca^{2+} oscillator of *S. purpuratus* spermatozoa expressed in temporal
910 delays. **b-d**. Gray points represent the collapsed data of all *f1*, *f2*, *f3*, *f4*, *f5* experimental
911 regimes. Red, black and blue points indicate chemotactic spermatozoa (LECI > 1),
912 located in R3, and R4 regions just before the speract gradient is established under *f2*, *f3*
913 and *f5* experimental regimes, respectively. Magenta lines represent the transition
914 boundary ($\gamma_{min} = \overline{\xi^*_{max}} \sim 2.7 \times 10^{-4}$) below which synchrony is not observed, obtained
915 from the theoretical estimates (black curves) of panels **c** and **d**. Green lines indicate
916 confidence intervals.

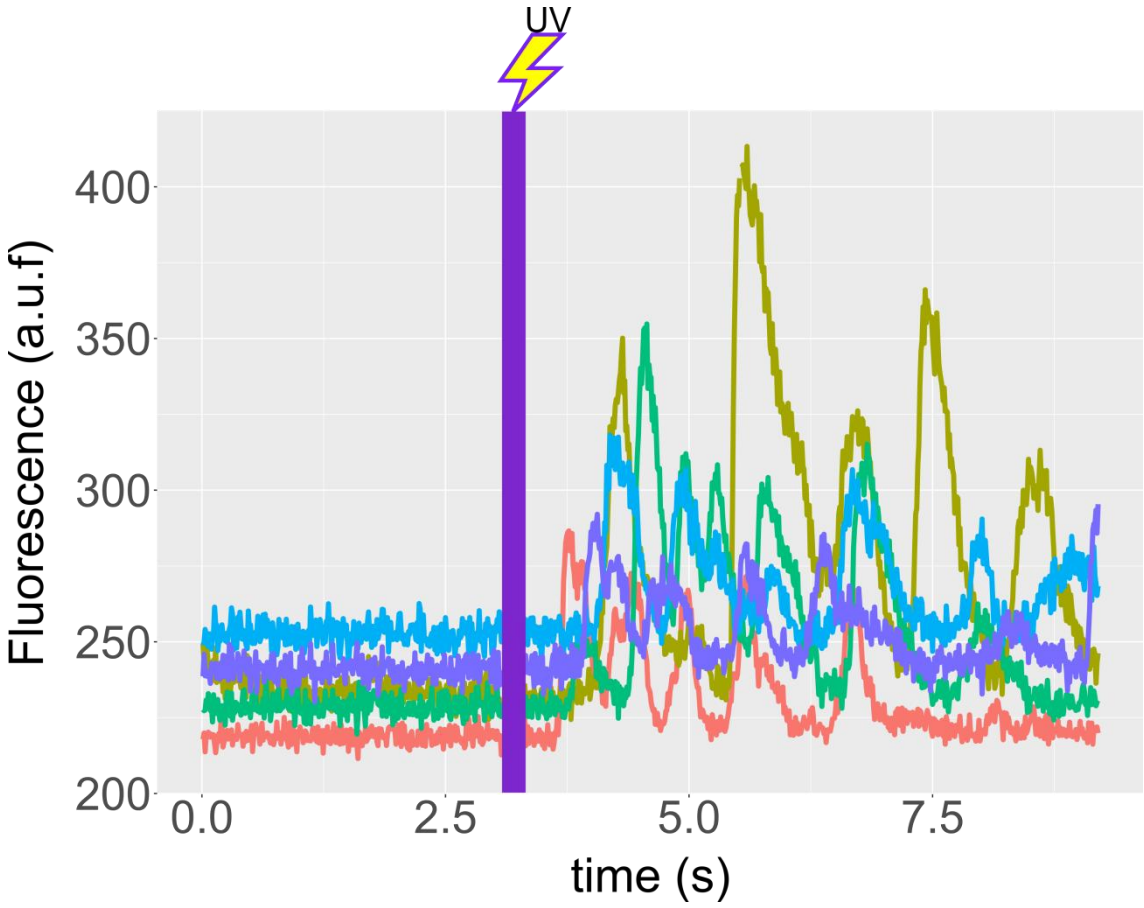

Figure 6 - figure supplement 1. Speract induces Ca^{2+} oscillations in immobilized *S. purpuratus* spermatozoa. Spermatozoa were immobilized on cover slips coated with poly-D-lysine (see **Materials and Methods**), and ASW containing 500 nM caged speract added. Recordings were performed 3s before and during 6s after 0.2s of UV irradiation. *f4* optical fiber was used for the UV light path, to generate the speract concentration gradient. The optical fiber was mounted on a "defocused" configuration to minimize UV light heterogeneities producing photoactivated speract gradients. Time traces indicate the $[Ca^{2+}]_i$ of selected spermatozoa of **Movie 8**. Note that the photo-release of speract induces a train of $[Ca^{2+}]_i$ episodes in immobilized spermatozoa, hence provides evidences for the presence of an internal Ca^{2+} oscillator triggered by speract.

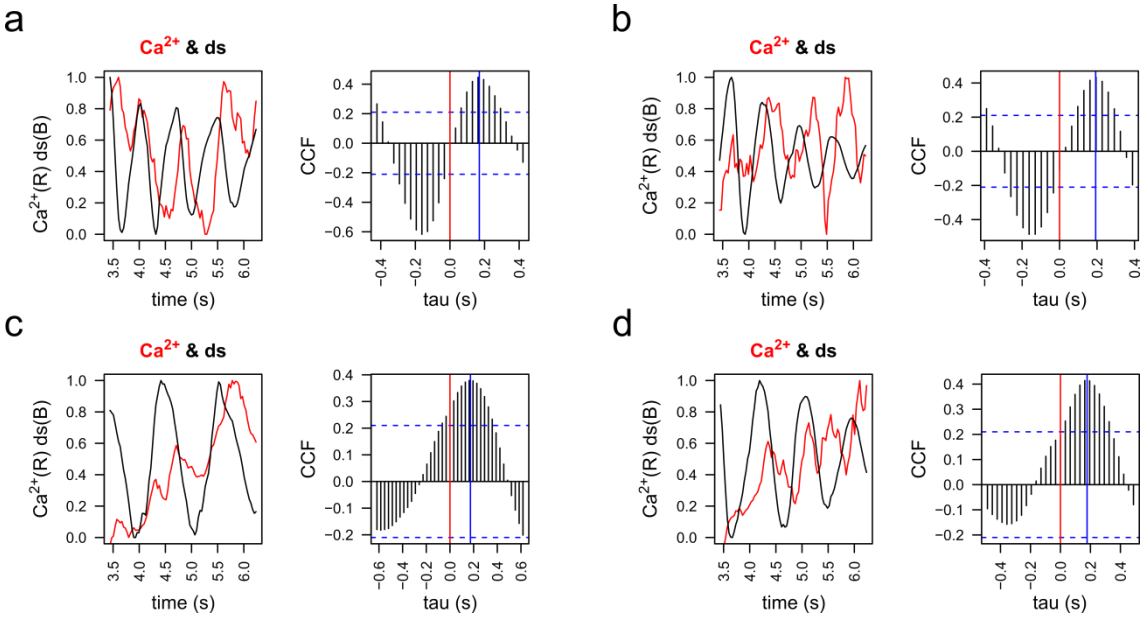

928

929 **Figure 6 - figure supplement 2. Cross-correlation analysis of $[Ca^{2+}]_i$ and stimulus**

930 **function derivative (ds) signals.** Representative examples of **[**$Ca^{2+}]_i$ and the derivate of

931 the stimulus function (ds) were plotted and then analyzed by cross-correlation analysis

932 (CCF). Examples of a pair of spermatozoa for the two principal chemotactic gradients

933 (*f2* and *f3*) are shown. **a, b.** Representative examples of two spermatozoa in *f2* gradient.

934 **c, d.** Representative examples of two spermatozoa in *f3* gradient.

935 **Movies**

936 https://www.dropbox.com/s/oe0mnc8j5r65l8s/Movie%201.avi?dl=0

937 **Movie 1. Typical motility and Ca^{2+} responses of *S. purpuratus* spermatozoa**
938 **towards *f2*-generated speract concentration gradient.** Spermatozoa swimming in
939 artificial sea water containing 10 nM caged speract, 3 s before and 5 s after 200 ms UV
940 irradiation. An optical fiber of 0.6 mm internal diameter was used for the UV light path
941 to generate the speract concentration gradient. Real time: 31 frames s^{-1}, 40x /1.3NA oil-
942 immersion objective. Note that spermatozoa located at R2, R3 and R4 regions prior
943 speract exposure swim up the speract concentration gradient, towards the center of the
944 imaging field. The pseudo-color scale represents the relative fluorescence of fluo-4, a
945 Ca^{2+} indicator, showing maximum (red) and minimum (blue) relative $[Ca^{2+}]_i$. Six *S.*
946 *purpuratus* spermatozoa were manually tracked for visualization purposes. Scale bar of
947 50 µm.

948 https://www.dropbox.com/s/v1h4kx6oqxc0f5l/Movie%202.avi?dl=0

949 **Movie 2. Typical motility and Ca^{2+} responses of *S. purpuratus* spermatozoa**
950 **towards *f3*-generated speract concentration gradient.** An optical fiber of 2 mm
951 internal diameter was used for the UV light path to generate the speract concentration
952 gradient. Other imaging conditions were set up as for Movie 1. Note that spermatozoa
953 located at R2, R3 and R4 regions prior to speract exposure swim up the speract
954 concentration gradient, towards the center of the imaging field. The pseudo-color scale
955 represents the relative fluorescence of fluo-4, a Ca^{2+} indicator, showing maximum (red)
956 and minimum (blue) relative $[Ca^{2+}]_i$. Six *S. purpuratus* spermatozoa were manually
957 tracked for visualization purposes. Scale bar of 50 µm.

https://www.dropbox.com/s/27v2i3ofda57fqs/Movie%203.avi?dl=0

Movie 3. Chemotaxis of *S. purpuratus* spermatozoa requires extracellular calcium. Spermatozoa swimming in artificial sea water with nominal calcium containing 10 nM caged speract 3 s before and 5 s after exposure to 200 ms UV light. Nominal calcium disrupts the electrochemical gradient required for Ca^{2+} influx, hence blocking the triggering of the internal Ca^{2+} oscillator by speract. The *f2* fiber (0.6 mm diameter) was used to uncage speract in this control. Other imaging conditions were set up as for Movie 1. Note that spermatozoa re-located after speract uncaging but they fail to experience the Ca^{2+}-driven motility alteration triggered by speract. As a consequence they fail to experience chemotaxis (compare with Movie 1). The pseudo-color scale represents the relative fluorescence of fluo-4, a Ca^{2+} indicator, showing maximum (red) and minimum (blue) relative $[Ca^{2+}]_i$. Six *S. purpuratus* spermatozoa were manually tracked for visualization purposes. Scale bar of 50 µm.

https://www.dropbox.com/s/vft4aiw96fpf3sy/Movie%204.avi?dl=0

Movie 4. Disrupting the K^+ electrochemical gradient blocks chemotaxis of *S. purpuratus* spermatozoa. Cells were swimming in artificial sea water containing 40 mM of KCl, and 10 nM caged speract 3 s before and 5 s after exposure to 200 ms UV light. High K^+ in the ASW blocks the hyperpolarization required for opening Ca^{2+} channels, and hence prevents the triggering of the internal Ca^{2+} oscillator by speract exposure. The *f2* fiber (0.6 mm diameter) was used to uncage speract in this control. Other imaging conditions were set up as for Movie 1. Note that spermatozoa re-located after speract uncaging but they fail to experience the Ca^{2+}-driven motility alteration triggered by speract, and thus they fail to experience chemotaxis (compare with Movie 1). The pseudo-color scale represents the relative fluorescence of fluo-4, a Ca^{2+} indicator, showing maximum (red) and minimum (blue) relative $[Ca^{2+}]_i$. Six *S. purpuratus* spermatozoa were manually tracked for visualization purposes. Scale bar of 50 µm.

985 https://www.dropbox.com/s/l3l7nmh1yw9juov/Movie%205.avi?dl=0

986 **Movie 5. Typical motility and Ca^{2+} responses of *S. purpuratus* spermatozoa**
987 **towards *f1*-generated speract concentration gradient.** An optical fiber of 0.2 mm
988 internal diameter was used for the UV light path to generate the speract concentration
989 gradient. Other imaging conditions were set up as for Movie 1. Note that some
990 spermatozoa re-located after speract uncaging but they fail to experience chemotaxis
991 (compare with Movie 1). The pseudo-color scale represents the relative fluorescence of
992 fluo-4, a Ca^{2+} indicator, showing maximum (red) and minimum (blue) relative $[Ca^{2+}]_i$.
993 Six *S. purpuratus* spermatozoa were manually tracked for visualization purposes. Scale
994 bar of 50 µm.

https://www.dropbox.com/s/qvwnyysbij6iz3b/Movie%206.avi?dl=0

Movie 6. Typical motility and Ca^{2+} responses of *S. purpuratus* spermatozoa towards *f4*-generated speract concentration gradient. An optical fiber of 4 mm internal diameter was used for the UV light path to generate the speract concentration gradient. Other imaging conditions were set up as for Movie 1. Note that spermatozoa re-located after speract uncaging but they fail to experience chemotaxis (compare with Movie 1). The pseudo-color scale represents the relative fluorescence of fluo-4, a Ca^{2+} indicator, showing maximum (red) and minimum (blue) relative $[Ca^{2+}]_i$. Six *S. purpuratus* spermatozoa were manually tracked for visualization purposes. Scale bar of 50 µm.

https://www.dropbox.com/s/o5o1e2jpmfitb1k/Movie%207.avi?dl=0

Movie 7. Typical motility and Ca^{2+} responses of *S. purpuratus* spermatozoa towards *f5*-generated speract concentration gradient. An optical fiber of 4 mm internal diameter was used for the UV light path to generate the speract concentration gradient. Other imaging conditions were set up as for Movie 1. Note that spermatozoa located at R2, R3 and R4 regions prior to speract exposure swim up the speract concentration gradient, towards the center of the imaging field. The pseudo-color scale represents the relative fluorescence of fluo-4, a Ca^{2+} indicator, showing maximum (red) and minimum (blue) relative $[Ca^{2+}]_i$. Six *S. purpuratus* spermatozoa were manually tracked for visualization purposes. Scale bar of 50 µm.

https://www.dropbox.com/s/dtfug8i1ckj6nku/Movie%208.avi?dl=0

Movie 8. Photo-release of caged speract induces Ca^{2+} oscillations in immobilized *S. purpuratus* spermatozoa. Spermatozoa were immobilized, by coating the cover slip with a thin layer of poly-D-lysine, in artificial sea water containing 500 nM caged speract, 3 s before and during 6 s after 0.2 s of UV irradiation. The *f4* optical fiber was used for the UV light path to generate the speract concentration gradient. The optical fiber was mounted on a "defocused" configuration to minimize the generation of UV light heterogeneities. 93 frames s^{-1}, 40x/1.3NA oil-immersion objective, 4x4 binning. The pseudo-color scale represents the relative fluorescence of fluo-4, a Ca^{2+} indicator, showing maximum (red) and minimum (blue) relative $[Ca^{2+}]_i$. The brightness and contrast scale was adjusted for better visualization of $[Ca^{2+}]_i$ transients in the sperm flagella (as a consequence some heads look artificially oversaturated, however no fluorescence saturation was observed in the raw data).

References

2011. R: A Language and Environment for Statistical Computing. Vienna, Austria : the R Foundation for Statistical Computing: R Development Core Team.

AGUILERA, L. U., GALINDO, B. E., SANCHEZ, D. & SANTILLAN, M. 2012. What is the core oscillator in the speract-activated pathway of the Strongylocentrotus purpuratus sperm flagellum? *Biophys J,* 102**,** 2481-8.

ALVAREZ, L., DAI, L., FRIEDRICH, B. M., KASHIKAR, N. D., GREGOR, I., PASCAL, R. & KAUPP, U. B. 2012. The rate of change in Ca(2+) concentration controls sperm chemotaxis. *J Cell Biol,* 196**,** 653-63.

AREF, H., BLAKE, J. R., BUDIŠIĆ, M., CARTWRIGHT, J. H. E., CLERCX, H. J. H., FEUDEL, U., GOLESTANIAN, R., GOUILLART, E., LE GUER, Y., VAN HEIJST, G. F., KRASNOPOLSKAYA, T. S., MACKAY, R. S., MELESHKO, V. V., METCALFE, G., MEZIĆ, I., DE MOURA, A. P. S., EL OMARI, K., PIRO, O., SPEETJENS, M. F. M., STURMAN, R., THIFFEAULT, J. L. & TUVAL, I. 2014. Frontiers of chaotic advection. *Reviews of Modern Physics,* 1403**,** 61.

BATCHELOR, G. K. 2006. Small-scale variation of convected quantities like temperature in turbulent fluid Part 1. General discussion and the case of small conductivity. *Journal of Fluid Mechanics,* 5**,** 113.

BERG, H. C. & PURCELL, E. M. 1977. Physics of chemoreception. *Biophys J,* 20**,** 193-219.

BOHMER, M., VAN, Q., WEYAND, I., HAGEN, V., BEYERMANN, M., MATSUMOTO, M., HOSHI, M., HILDEBRAND, E. & KAUPP, U. B. 2005. Ca2+ spikes in the flagellum control chemotactic behavior of sperm. *EMBO J,* 24**,** 2741-52.

BROKAW, C. J. 1979. Calcium-induced asymmetrical beating of triton-demembranated sea urchin sperm flagella. *J Cell Biol,* 82**,** 401-11.

COOK, S. P., BROKAW, C. J., MULLER, C. H. & BABCOCK, D. F. 1994. Sperm chemotaxis: egg peptides control cytosolic calcium to regulate flagellar responses. *Dev Biol,* 165**,** 10-9.

DARSZON, A., GUERRERO, A., GALINDO, B. E., NISHIGAKI, T. & WOOD, C. D. 2008. Sperm-activating peptides in the regulation of ion fluxes, signal transduction and motility. *Int J Dev Biol,* 52**,** 595-606.

DUSENBERY, D. B. 2011. *Living at micro scale: The unexpected physics of being small*, Harvard University Press.

ESPINAL, J., ALDANA, M., GUERRERO, A., WOOD, C., DARSZON, A. & MARTINEZ-MEKLER, G. 2011. Discrete dynamics model for the speract-activated Ca2+ signaling network relevant to sperm motility. *PLoS One,* 6**,** e22619.

FRIEDRICH, B. M. & JÜLICHER, F. 2007. Chemotaxis of sperm cells. *Proc Natl Acad Sci U S A,* 104**,** 13256-61.

FRIEDRICH, B. M. & JÜLICHER, F. 2008. The stochastic dance of circling sperm cells: sperm chemotaxis in the plane. *New Journal of Physics,* 10**,** 123025.

FRIEDRICH, B. M. & JÜLICHER, F. 2009. Steering chiral swimmers along noisy helical paths. *Phys Rev Lett,* 103**,** 068102.

GARCES, Y., GUERRERO, A., HIDALGO, P., LOPEZ, R. E., WOOD, C. D., GONZALEZ, R. A. & RENDON-MANCHA, J. M. 2016. Automatic detection and measurement of viral replication compartments by ellipse adjustment. *Sci Rep,* 6**,** 36505.

GUERRERO, A., NISHIGAKI, T., CARNEIRO, J., YOSHIRO, T., WOOD, C. D. & DARSZON, A. 2010a. Tuning sperm chemotaxis by calcium burst timing. *Dev Biol,* 344**,** 52-65.

GUERRERO, A., WOOD, C. D., NISHIGAKI, T., CARNEIRO, J. & DARSZON, A. 2010b. Tuning sperm chemotaxis. *Biochem Soc Trans,* 38**,** 1270-4.

HANSBROUGH, J. R. & GARBERS, D. L. 1981. Speract. Purification and characterization of a peptide associated with eggs that activates spermatozoa. *J Biol Chem,* 256**,** 1447-52.

HUSSAIN, Y. H., SADILEK, M., SALAD, S., ZIMMER, R. K. & RIFFELL, J. A. 2017. Individual female differences in chemoattractant production change the scale of sea urchin gamete interactions. *Dev Biol,* 422**,** 186-197.

JIKELI, J. F., ALVAREZ, L., FRIEDRICH, B. M., WILSON, L. G., PASCAL, R., COLIN, R., PICHLO, M., RENNHACK, A., BRENKER, C. & KAUPP, U. B. 2015. Sperm navigation along helical paths in 3D chemoattractant landscapes. *Nat Commun,* 6**,** 7985.

JIMÉNEZ, J. 1997. Oceanic turbulence at millimeter scales. *Scientia Marina,* 61**,** 47-56.

KASHIKAR, N. D., ALVAREZ, L., SEIFERT, R., GREGOR, I., JACKLE, O., BEYERMANN, M., KRAUSE, E. & KAUPP, U. B. 2012. Temporal sampling, resetting, and adaptation orchestrate gradient sensing in sperm. *J Cell Biol,* 198**,** 1075-91.

KAUPP, U. B. 2012. 100 years of sperm chemotaxis. *J Gen Physiol,* 140**,** 583-6.

KAUPP, U. B., KASHIKAR, N. D. & WEYAND, I. 2008. Mechanisms of sperm chemotaxis. *Annu Rev Physiol,* 70**,** 93-117.

KAUPP, U. B., SOLZIN, J., HILDEBRAND, E., BROWN, J. E., HELBIG, A., HAGEN, V., BEYERMANN, M., PAMPALONI, F. & WEYAND, I. 2003. The signal flow and motor response controling chemotaxis of sea urchin sperm. *Nat Cell Biol,* 5**,** 109-17.

LAKOWICZ, J. R. 2006. *Principles of Fluorescence Spectroscopy,* Springer US.

LILLIE, F. R. 1913. The mechanism of fertilization. *Science,* 38**,** 524-528.

LOTTERHOS, K. E. L., D. R 2010. *Gamete release and spawning behavior in broadcast spawning marine invertebrates,* New York, NY, Oxford University Press.

MAUPETIT, J., DERREUMAUX, P. & TUFFERY, P. 2009. PEP-FOLD: an online resource for de novo peptide structure prediction. *Nucleic Acids Res,* 37**,** W498-503.

MAUPETIT, J., DERREUMAUX, P. & TUFFERY, P. 2010. A fast method for large-scale de novo peptide and miniprotein structure prediction. *J Comput Chem,* 31**,** 726-38.

MEAD, K. S. & DENNY, M. W. 1995. The effects of hydrodynamic shear stress on fertilization and early development of the purple sea urchin Strongylocentrotus purpuratus. *Biol Bull,* 188**,** 46-56.

MEIJERING, E., DZYUBACHYK, O. & SMAL, I. 2012. Methods for cell and particle tracking. *Methods Enzymol,* 504**,** 183-200.

MILLER, R. L. 1985. Sperm Chemo-Orientation in the Metazoa. *In:* METZ, C. B. & MONROY, A. (eds.) *Biology of Fertilization.* New York: Academic Press.

NISHIGAKI, T. & DARSZON, A. 2000. Real-time measurements of the interactions between fluorescent speract and its sperm receptor. *Dev Biol,* 223**,** 17-26.

NISHIGAKI, T., ZAMUDIO, F. Z., POSSANI, L. D. & DARSZON, A. 2001. Time-resolved sperm responses to an egg peptide measured by stopped-flow fluorometry. *Biochem Biophys Res Commun,* 284**,** 531-5.

PETTERSEN, E. F., GODDARD, T. D., HUANG, C. C., COUCH, G. S., GREENBLATT, D. M., MENG, E. C. & FERRIN, T. E. 2004. UCSF Chimera--a visualization system for exploratory research and analysis. *J Comput Chem,* 25**,** 1605-12.

PFEFFER, W. 1884. Locomotorische Richtungsbewegungen durch chemische Reize. *In Untersuchungen aus dem botanischen Institut zu Tübingen,* 1**,** 363-482.

PICHLO, M., BUNGERT-PLUMKE, S., WEYAND, I., SEIFERT, R., BONIGK, W., STRUNKER, T., KASHIKAR, N. D., GOODWIN, N., MULLER, A., PELZER, P., VAN, Q., ENDERLEIN, J., KLEMM, C., KRAUSE, E., TROTSCHEL, C., POETSCH, A., KREMMER, E., KAUPP, U. B., KORSCHEN, H. G. & COLLIENNE, U. 2014. High density and ligand affinity confer ultrasensitive signal detection by a guanylyl cyclase chemoreceptor. *J Cell Biol,* 206**,** 541-57.

PIKOVSKY, A., ROSENBLUM, M. & KURTHS, J. 2001. *Synchronization. A Universal Concept in Nonlinear Sciences,* Cambridge University Press; 1 edition.

RIFFELL, J. A. & ZIMMER, R. K. 2007. Sex and flow: the consequences of fluid shear for sperm-egg interactions. *J Exp Biol,* 210**,** 3644-60.

SCHNEIDER, C. A., RASBAND, W. S. & ELICEIRI, K. W. 2012. NIH Image to ImageJ: 25 years of image analysis. *Nat Methods,* 9**,** 671-5.

SHIBA, K., BABA, S. A., INOUE, T. & YOSHIDA, M. 2008. Ca2+ bursts occur around a local minimal concentration of attractant and trigger sperm chemotactic response. *Proc Natl Acad Sci U S A,* 105**,** 19312-7.

SHIMOMURA, H. & GARBERS, D. L. 1986. Differential effects of resact analogues on sperm respiration rates and cyclic nucleotide concentrations. *Biochemistry,* 25**,** 3405-10.

SMITH, A. C. & GARBERS, D. L. 1983. The binding of an 125I-speract analogue to spermatozoa. *In:* LENNON, D. L., STRATMAN, F. W. & ZAHLTEN, R. N., eds. Biochemistry of Metabolic Processes, 1982 Madison, Wisconsin, U.S.A. Amsterdam, New York, U.S.A.: Elsevier, 496.

STRUNKER, T., ALVAREZ, L. & KAUPP, U. B. 2015. At the physical limit - chemosensation in sperm. *Curr Opin Neurobiol,* 34**,** 110-6.

SUZUKI, N. 1995. Structure, function and biosynthesis of sperm-activating peptides and fucose sulfate glycoconjugate in the extracellular coat of sea urchin eggs. *Zoolog Sci,* 12**,** 13-27.

TATSU, Y., NISHIGAKI, T., DARSZON, A. & YUMOTO, N. 2002. A caged sperm-activating peptide that has a photocleavable protecting group on the backbone amide. *FEBS Lett,* 525**,** 20-4.

THEVENET, P., SHEN, Y., MAUPETIT, J., GUYON, F., DERREUMAUX, P. & TUFFERY, P. 2012. PEP-FOLD: an updated de novo structure prediction server for both linear and disulfide bonded cyclic peptides. *Nucleic Acids Res,* 40**,** W288-93.

THORPE, S. A. 2007. *An Introduction to Ocean Turbulence,* Cambridge University Press.

VERGASSOLA, M., VILLERMAUX, E. & SHRAIMAN, B. I. 2007. 'Infotaxis' as a strategy for searching without gradients. *Nature,* 445**,** 406-9.

WOOD, C. D., DARSZON, A. & WHITAKER, M. 2003. Speract induces calcium oscillations in the sperm tail. *J Cell Biol,* 161**,** 89-101.

WOOD, C. D., GUERRERO, A., PRIEGO-ESPINOSA, D. A., MARTÍNEZ-MEKLER, G., CARNEIRO, J. & DARSZON, A. 2015. Sea Urchin Sperm Chemotaxis. *In:*

COSSON, J. J. (ed.) *Flagellar Mechanics and Sperm Guidance.* Czech Republic: Bentham Science Publishers.

WOOD, C. D., NISHIGAKI, T., FURUTA, T., BABA, S. A. & DARSZON, A. 2005. Real-time analysis of the role of Ca(2+) in flagellar movement and motility in single sea urchin sperm. *J Cell Biol,* 169**,** 725-31.

WOOD, C. D., NISHIGAKI, T., TATSU, Y., YUMOTO, N., BABA, S. A., WHITAKER, M. & DARSZON, A. 2007. Altering the speract-induced ion permeability changes that generate flagellar Ca2+ spikes regulates their kinetics and sea urchin sperm motility. *Dev Biol,* 306**,** 525-37.

YOSHIDA, M., MURATA, M., INABA, K. & MORISAWA, M. 2002. A chemoattractant for ascidian spermatozoa is a sulfated steroid. *Proc Natl Acad Sci U S A,* 99**,** 14831-6.

ZIMMER, R. K. & RIFFELL, J. A. 2011. Sperm chemotaxis, fluid shear, and the evolution of sexual reproduction. *Proc Natl Acad Sci U S A,* 108**,** 13200-5.